Clim. Past Discuss., 11, 3277–3339, 2015
www.clim-past-discuss.net/11/3277/2015/
doi:10.5194/cpd-11-3277-2015

Climate of the Past Discussions
Open Access

Insights into the early Eocene hydrological cycle from an ensemble of atmosphere–ocean GCM simulations

M. J. Carmichael[1,2], D. J. Lunt[1], M. Huber[3], M. Heinemann[4], J. Kiehl[5], A. LeGrande[6], C. A. Loptson[1], C. D. Roberts[7], N. Sagoo[1,a], C. Shields[5], P. J. Valdes[1], A. Winguth[8], C. Winguth[8], and R. D. Pancost[2]

[1]BRIDGE, School of Geographical Sciences and Cabot Institute, University of Bristol, UK
[2]Organic Geochemistry Unit, School of Chemistry and Cabot Institute, University of Bristol, UK
[3]Climate Dynamics Prediction Laboratory, Department of Earth Sciences, The University of New Hampshire, USA
[4]International Pacific Research Center, School of Ocean and Earth Science and Technology, University of Hawaii, USA
[5]Climate and Global Dynamics Laboratory, UCAR/NCAR, USA
[6]NASA Goddard Institute for Space Studies, USA
[7]The Met Office, UK
[8]Climate Research Group, Department of Earth and Environmental Sciences, University of Texas Arlington, USA
[a]now at: Department of Geology and Geophysics, Yale University, USA

Received: 19 June 2015 – Accepted: 25 June 2015 – Published: 17 July 2015

Correspondence to: M. J. Carmichael (matt.carmichael@bristol.ac.uk)

Published by Copernicus Publications on behalf of the European Geosciences Union.

Abstract

Recent studies, utilising a range of proxies, indicate that a significant perturbation to global hydrology occurred at the Paleocene–Eocene Thermal Maximum (PETM; ~ 56 Ma). An enhanced hydrological cycle for the warm early Eocene is also suggested to have played a key role in maintaining high-latitude warmth during this interval. However, comparisons of proxy data to General Circulation Model (GCM) simulated hydrology are limited and inter-model variability remains poorly characterised, despite significant differences in simulated surface temperatures. In this work, we undertake an intercomparison of GCM-derived precipitation and $P - E$ distributions within the EoMIP ensemble (Lunt et al., 2012), which includes previously-published early Eocene simulations performed using five GCMs differing in boundary conditions, model structure and precipitation relevant parameterisation schemes.

We show that an intensified hydrological cycle, manifested in enhanced global precipitation and evaporation rates, is simulated for all Eocene simulations relative to preindustrial. This is primarily due to elevated atmospheric paleo-CO_2, although the effects of differences in paleogeography/ice sheets are also of importance in some models. For a given CO_2 level, globally-averaged precipitation rates vary widely between models, largely arising from different simulated surface air temperatures. Models with a similar global sensitivity of precipitation rate to temperature (dP/dT) display different regional precipitation responses for a given temperature change. Regions that are particularly sensitive to model choice include the South Pacific, tropical Africa and the Peri-Tethys, which may represent targets for future proxy acquisition.

A comparison of early and middle Eocene leaf-fossil-derived precipitation estimates with the GCM output illustrates that a number of GCMs underestimate precipitation rates at high latitudes. Models which warm these regions, either via elevated CO_2 or by varying poorly constrained model parameter values, are most successful in simulating a match with geologic data. Further data from low-latitude regions and better constraints on early Eocene CO_2 are now required to discriminate between these model

CPD
11, 3277–3339, 2015

simulations given the large error bars on paleoprecipitation estimates. Given the clear differences apparent between simulated precipitation distributions within the ensemble, our results suggest that paleohydrological data offer an independent means by which to evaluate model skill for warm climates.

1 Introduction

Considerable uncertainty exists in understanding how the Earth's hydrological cycle will function on a future warmer-than-present planet. State-of-the-art General Circulation Models (GCMs) show a wide inter-model spread for future precipitation and runoff responses when prescribed with the same greenhouse gas emission trajectories (IPCC, 2013; Knutti and Sedláček, 2012). Remarkably few studies have investigated the hydrology of ancient greenhouse climates, but understanding how the hydrological cycle operated differently during these intervals could provide insight into the mechanisms which will govern future changes and the sensitivity of these processes (e.g. Pierrehumbert, 2002; Suarez et al., 2009; White et al., 2001). In particular, characterising the hydrological cycle simulated in GCMs using paleo-boundary conditions and comparisons to geological proxy data can contribute to developing an understanding of how well models that are used to make future predictions perform for warm climates.

The early Eocene (~ 56–49 Ma) represents the warmest sustained interval of the Cenozoic, with evidence for substantially elevated global temperatures relative to modern in both marine (Zachos et al., 2008; Dunkley Jones et al., 2013) and terrestrial settings (Huber and Caballero, 2011; Pancost et al., 2013). This is particularly evident at high latitudes: pollen and macrofossil evidence indicate near-tropical forest growth on Antarctica during the Early Eocene Climatic Optimum (EECO; Pross et al., 2012; Francis et al., 2008) and fossils of fauna including alligators, tapirs and non-marine turtles occur in the Canadian Arctic (Markwick, 1998; Eberle, 2005; Eberle and Greenwood, 2012). Absolute temperatures for the Paleogene remain controversial (e.g. Taylor et al., 2013; Douglas et al., 2014; Hollis et al., 2012), but quantitative estimates from

CPD
11, 3277–3339, 2015

multiple proxies support substantial global warmth. Mean annual Sea Surface Temperature (SST) for the Arctic has been estimated at ~ 17–18 °C rising to ~ 23 °C during the Paleocene–Eocene Thermal Maximum (PETM) hyperthermal at 56 Ma (TEX86'; Sluijs et al., 2006). SSTs may have reached 26–28 °C in the Southwest Pacific during the Early Eocene Climatic Optimum (EECO, TEX_{86}^{L}; Hollis et al., 2012; Bijl et al., 2009). EECO Mean Air Temperature (MAT) of Wilkes' Land margin on Antarctica has been estimated at 16 ± 5 °C (Nearest Living Relative, NLR, based on paratropical vegetation), with summer temperatures as high as 24–27 °C, inferred from soil bacterial tetraether lipids (MBT/CBT; Pross et al., 2012); similar but slightly higher MATs were obtained from New Zealand (Pancost et al., 2013). Low latitude data are scarce, but oxygen istopes of planktic foraminfera and TEX_{86} indicate SSTs off the coast of Tanzania > 30 °C (Pearson et al., 2007; Huber, 2008).

Few proxy estimates of early Eocene atmospheric carbon dioxide exist. Paleosol geochemistry indicates concentrations could have reached ~ 3000 ppmv (Yapp, 2004; Lowenstein and Demicco, 2006), whilst stomatal index approaches yield more modest values of 400–600 ppmv (Royer et al., 2001; Smith et al., 2010). Recent modelling indicates that terrestrial methane emissions also could have been significantly greater than modern, representing an additional greenhouse gas forcing (Beerling et al., 2011). GCM simulations with greenhouse gas concentrations substantially elevated compared to modern have had greatest success in reproducing proxy-inferred warmth (Huber and Caballero, 2011; Lunt et al., 2012), providing further evidence that global Eocene warmth was maintained by elevated concentrations of greenhouse gases. However, simulating warm high latitude and equable continental interior temperatures remains a challenge, with models struggling to replicate the reduced equator-pole temperature gradient implied by the proxies (Huber and Sloan, 2001; Valdes, 2011; Pagani et al., 2013 and references therein). This has resulted in suggestions that GCMs may be missing key heat transfer processes, new modelling aimed at reducing data-model anomalies, as well as re-evaluations of existing proxy data (Sagoo et al., 2013; Kiehl

CPD
11, 3277–3339, 2015

and Shields, 2013; Loptson et al., 2014; Sluijs et al., 2006; Huber and Caballero, 2011; Lunt et al., 2012).

The hydrology of this super-greenhouse climate state remains poorly characterised. Initial observations of globally widespread Eocene laterites and coals (Frakes, 1979; Sloan et al., 1992) and of enhanced sedimentation rates and elevated kaolinite in the clay fraction of many coastal sections (Bolle et al., 2000; Bolle and Adatte, 2001; John et al., 2012; Robert and Kennett, 1994; Nicolo et al., 2007) suggested early Eocene terrestrial environments were characterised by globally enhanced precipitation and runoff relative to today. Diverse geochemical proxies are now providing a more nuanced interpretation of how the spatial organisation of the Eocene hydrological cycle differed from that of the modern. This is particularly the case for the PETM. In the Arctic, the hydrogen isotopic composition of putative leaf-wax compounds is enriched by ~ 55 ‰ δD at the PETM, thought to reflect increased export of moisture from low latitudes (Pagani et al., 2006). Enrichment of δD in leaf waxes from tropical Tanzania, coincident with elevated concentrations of terrestrial biomarkers and sedimentation rates, has been interpreted as indicating a shift to a more arid climate with seasonally heavy rainfall (Handley et al., 2012, 2008). Whether these changes are typical of the low latitudes or are highly localised responses remains to be determined. Elsewhere, conflicting evidence for regional hydrological changes exist: an increased PETM offset in the magnitude of the Carbon Isotope Exursion (CIE) between marine and terrestrially-derived carbonates, including from Wyoming, has been suggested to reflect increases in humidity/soil moisture of the order of 20–25 % (Bowen et al., 2004). Other studies utilising leaf physiogonomy and paleosols suggest the North American continental interior became drier at the onset of the PETM, or alternated between wet and dry phases (Kraus et al., 2013; Smith et al., 2007; Wing et al., 2005).

Despite these indications of a background early Eocene hydrological cycle different to modern, and of significant hydrological changes at the PETM, only limited proxy-model comparisons have been made for the early Eocene hydrological cycle (Pagani et al., 2006; Speelman et al., 2010; Winguth et al., 2010). Some analysis of model

CPD
11, 3277–3339, 2015

sensitivity of precipitation and $P-E$ to imposed CO_2 (Winguth et al., 2010), paleogeography (e.g. Roberts et al., 2009) and parametric uncertainty (Sagoo et al., 2013; Kiehl and Shields, 2013) has been undertaken, but the range of hydrological behaviour simulated within different models has not yet been assessed. Lunt et al. (2012) undertook a model intercomparison of early Eocene warmth, EoMIP, based on an ensemble of 12 Eocene simulations undertaken in four fully-coupled atmosphere–ocean climate models, a summary of which is given in Table 1. This demonstrated differences in global surface air temperature of up to 9 °C for a single imposed CO_2 and differing regions of CO_2-induced warming, but the implications for the hydrological cycle have not been considered.

This study addresses three main questions: (1) how do globally averaged GCM precipitation rates for the Eocene compare to preindustrial simulations and vary between models in the EoMIP ensemble? (2) How consistently do the EoMIP GCMs simulate regional precipitation and $P-E$ distributions? (3) Do differences between models affect the degree of match with existing proxy estimates for mean annual precipitation?

2 Model descriptions

The EoMIP approach of Lunt et al. (2012) is distinct from formal model intercomparison projects which utilise a common experimental design (e.g. PMIP3, Taylor et al., 2012; CMIP5, Braconnot et al., 2012). Instead, the EoMIP models differ in their boundary conditions and span a plausible early Eocene CO_2 range, utilise different paleogeographic reconstructions and specify different vegetation distributions. This is in addition to internal differences in model structure and physics, including precipitation-relevant parameterisations such as those relating to convection and cloud microstructure. Whilst this may hinder the identification of reasons for inter-model differences, the ensemble spans more fully the uncertainty in boundary conditions, which is appropriate for deep-time climates such as the early Eocene.

CPD
11, 3277–3339, 2015

The ensemble, summarised in Table 1, includes a range of published simulations of the early Eocene carried out with fully dynamic atmosphere–ocean GCMs. We extend the EoMIP ensemble as originally described by Lunt et al. (2012) to include simulations published by Sagoo et al. (2013), Kiehl and Shields (2013) and Loptson et al. (2014). A brief description of each model and the corresponding simulation is given below. Each model produces large-scale (stratiform) and convective precipitation separately, also summarised in Table 1.

2.1 HadCM3L

HadCM3L is a version of the GCM developed by the UK Met Office (Cox et al., 2000). Eocene simulations performed with atmospheric CO_2 at ×2, ×4 and ×6 preindustrial levels were presented by Lunt et al. (2010) in their study of the role of ocean circulation as a possible PETM trigger via methane hydrate destabilisation. In these simulations, models were integrated for more than 3400 years to allow intermediate-depth ocean temperatures to equilibrate. Both the atmosphere and ocean are discretised on a 3.75° longitude × 2.5° latitude grid, with 19 vertical levels in the atmosphere and 20 in the ocean. Vegetation is set to a globally homogenous shrubland.

The effect of using an interactive vegetation model, TRIFFID (Cox, 2001), on temperature proxy-model anomalies was considered by Loptson et al. (2014) who performed simulations at ×2 and ×4 CO_2, continuations of those of Lunt et al. (2010). This study indicated that for a given prescribed CO_2, the inclusion of dynamic vegetation acts to warm global climate via albedo and water vapour feedbacks. We refer to these simulations as HadCM3L_T. The effect of dynamic vegetation on precipitation distributions and global precipitation rate was additionally briefly considered but comparisons to precipitation proxy data or to other models have not been undertaken.

CPD
11, 3277–3339, 2015

2.2 FAMOUS

FAMOUS is an alternative version of the UK Met Office's GCM, adopting the same climate parameterisations as HadCM3L, but solved at a reduced spatial and temporal resolution in the atmosphere (Jones et al., 2005; Smith et al., 2008). Atmospheric resolution is 7.5° longitude × 5° latitude, with 11 levels in the vertical, whilst the ocean resolution matches that of HadCM3L. Both modules operate at an hourly time-step. Because of its reduced resolution, FAMOUS has been used for transient simulations with long run-times and in perturbed parameter ensembles where a large number of simulations are required (Smith and Gregory, 2012; Williams et al., 2013). Sagoo et al. (2013) used FAMOUS to study the effect of parametric uncertainty on early Eocene temperature distributions by varying 10 climatic parameters which are typically poorly constrained in climate models. Their results demonstrated that a globally warm climate with a reduced equator-to-pole temperature gradient can be achieved at 2 × preindustrial CO_2. Of the seventeen successful simulations which ran to completion, our focus is on E16 and E17, the simulations with the shallowest equator-to-pole temperature gradient and which show the optimal match to marine and terrestrial temperature proxy-data. At the ocean grid resolution, the paleogeography matches that of Lunt et al. (2010). Vegetation is set to a homogenous shrubland. All simulations were run for a minimum of 8000 model years and full details of the perturbed parameters are provided in Sagoo et al. (2013). Sagoo et al. show DJF and JJA precipitation distributions for their globally warmest and coolest simulations, but comparisons to other models or to proxy data have not been made.

2.3 CCSM3

We utilise three sets of simulations performed with CCSM3, a GCM developed by the US National Centre for Atmospheric Research in collaboration with the university community (Collins et al., 2006). The first set were initially used by Liu et al. (2009) in their study of Eocene–Oligocene sea surface temperatures, and subsequently compared

CPD
11, 3277–3339, 2015

to terrestrial proxy data in a study of the early Eocene climate equability problem by Huber and Caballero (2011). These simulations are configured with atmospheric CO_2 at ×2, ×4, ×8 and ×16 preindustrial. Models were integrated for between 2000 and 5000 years, until the sea surface temperature was in equilibrium. The atmosphere is resolved on a 3.75° longitude by ∼ 3.75 latitude (T31) grid with 26 levels in the vertical and the ocean is resolved on an irregularly spaced dipole grid. The prescribed land surface cover follows the reconstructed vegetation distribution utilised in Sewall et al. (2000). Following the approach of Lunt et al. (2012) we refer to these simulations as CCSM3_H.

The second set of simulations, which we refer to as CCSM3_W, were described by Winguth et al. (2010) and Shellito et al. (2009) and conducted at ×4, ×8 and ×16 preindustrial CO_2. Relative to the CCSM3_H simulations, these simulations utilised a solar constant reduced by 0.44 %, were integrated for a shorter period (∼ 1500 years), adopted an updated vegetation distribution (Shellito and Sloan, 2006) and utilised a marginal sea parameterisation, resulting in paleogeographic differences, particularly in polar regions. However, the major difference between the simulations is that the CCSM3_W simulations utilise a modern-day aerosol distribution, whereas CCSM3_H adopts a reduced loading for the early Eocene based on a hypothesised lower early Eocene ocean productivity (Kump and Pollard, 2008; Winguth et al., 2012). However, the extent to which increased volcanism at the PETM might have increased aerosol loading remains uncertain (Svensen et al., 2004; Storey et al., 2007).

The third set of simulations, CCSM3_K, are described in Kiehl and Shields (2013). This study investigated the sensitivity of Eocene climatology to the parameterisation of aerosol and cloud effects, specifically by altering cloud microphysical parameters including cloud drop number and effective cloud drop radii. Modern day values from pristine regions are applied homogenously across land and ocean. Simulations were performed at two greenhouse gas concentrations corresponding to possible pre- and trans-PETM atmospheric compositions which are equivalent to CO_2 of ∼ ×5 and ∼ ×9 preindustrial, respectively. Paleogeography and vegetation distribution are the same

CPD
11, 3277–3339, 2015

as those used in CCSM3_W and the solar constant is reduced by 0.487 % relative to modern. Changes in precipitation distribution between high- and low-CO_2 simulations have previously been shown for the CCSM3_W and CCSM3_K simulations (Winguth et al., 2010; Kiehl and Shields, 2013), but how robust these Eocene distributions are to GCM choice remains unknown.

2.4 ECHAM5/MPI-OM

The ECHAM5/MPI-OM model is the GCM of the Max Planck Institute for Meteorology (Roeckner et al., 2003), used by Heinemann et al. (2009) in their study of reasons for early Eocene warmth. The model was configured with CO_2 at ×2 preindustrial, using the paleogeography of Bice and Marotzke (2001) and a globally homogenous vegetation cover, with lower albedo but larger leaf area and forest fraction than pre-industrial, equivalent to a modern day woody savannah. Atmosphere components are resolved on a gaussian grid with a spacing of 3.75° longitude and approximately 3.75° latitude. Relative to the preindustrial simulation, methane is increased from 65 to 80 ppb and nitrous oxide from 270 to 288 ppb for the Eocene, but these are negligible relative to change in radiative forcing associated with doubling of preindustrial CO_2. Latitudinal precipitation distributions in the simulation relative to preindustrial were considered by Heinemann et al. (2009) and elevated convective precipitation at high-latitudes suggested to be consistent with convective clouds as a high latitudes warming mechanism (Abbot and Tziperman, 2008).

2.5 GISS-ER

The E-R version of the Goddard Institute for Space Studies model (GISS-ER; Schmidt et al., 2006) was utilised by Roberts et al. (2009) in their study of the impact of Arctic paleogeography on high latitude early Eocene sea surface temperature and salinity. Here, we include the simulation with open Arctic paleogeography of Bice and Marotzke (2001) which is also utilised in the ECHAM5 simulation. The simulation was forced

CPD
11, 3277–3339, 2015

with CO_2 at 4× preindustrial, and CH_4 at 7× preindustrial, equivalent of a total Eocene greenhouse gas forcing of ∼ 4.3× preindustrial CO_2. The atmospheric component of GISS-ER has a grid resolution of 4° latitude by 5° longitude with 20 levels in the vertical; the ocean model is of the same horizontal resolution but with 13 levels. Vegetation is prescribed as in Sewall et al. (2000). The hydrological cycle is shown to be intensified for the Paleogene simulation, with elevated global precipitation and evaporation rates, but spatial precipitation distributions were not studied.

3 Results

3.1 Preindustrial simulations

The simulation of precipitation is a particular challenge for GCMs given the range of spatial and temporal scales at which precipitation-producing processes occur, compared to a typical model grid and timestep (e.g. Knutti and Sedlacek, 2013; Hagemann et al., 2006). Model resolution and the parameterisation schemes which account for sub-grid scale precipitation, in addition to temperature distributions, differ between the GCMs in the ensemble (Table 1). We initially summarise model skill in simulating preindustrial Mean Annual Precipitation (MAP) to provide context for our Eocene model intercomparison and to identify which, if any, precipitation structures are unique to the Eocene, and which are more fundamentally related to errors particular to a given GCM.

Figure 1 shows preindustrial MAP distributions for each GCM in the EoMIP ensemble and anomalies for each preindustrial simulation relative to CMAP observations (Centre for Climate Prediction, Merged Analysis of Precipitation), which incorporates both satellite and gauge data (Yin et al., 2004; Gruber et al., 2000). The following observations can be made:

i. All of the EoMIP GCMs simulate the principal features of the observed preindustrial MAP distribution, although errors occur in their position and strength. The Inter-tropical Convergence Zone (ITCZ), North Atlantic and North Pacific storm

CPD
11, 3277–3339, 2015

stracks and subtropical precipitation minima in eastern ocean basins are identifiable for each simulation, but differences are evident between the models. Some biases are common to a number of the models, in particular those relating to the ITCZ and tropical precipitation. HadCM3L, FAMOUS, ECHAM5 and CCSM3 all simulate the ITCZ mean annual location north of the Equator, but the South Pacific Convergence Zone (SPCZ) generally extends too far east in the Pacific, and is too zonal, with precipitation equalling that to the north of the Equator to produce a "double-ITCZ" – a common bias in GCMs (Dai, 2006; Randall et al., 2007). The localised rain belt minimum is a result of the Pacific cold-tongue, not present in GISS-ER, which instead simulates a single convergence zone with high mean annual precipitation across the tropics. Other biases which appear common across the ensemble include over-precipitation in the Southern Ocean and too little precipitation over the Amazon and Antarctica (Hack et al., 2006; Randall et al., 2007 and references therein).

ii. Errors over the continents are less than those over the oceans. Absolute errors in MAP are largest over the high precipitation tropical and subtropical oceans, and frequently exceed 150 cm year^{-1} in the case of ITCZ and SPCZ offsets. Over the continents, anomalies are generally no greater than 60 cm year^{-1} and more than 80 % of the multimodel mean terrestrial surface has an anomaly less than 30 cm year^{-1}. In low precipitation regions, these errors could still result in significant percentage errors (Fig. S1).

iii. Models show regional differences in precipitation skill. Figure 1 demonstrates that some precipitation biases are individual to particular GCMs. Whilst these are most noticeable over the high precipitation tropical and subtropical oceans, such as offsets in the location of maximum precipitation intensity or strength of storm tracks, relative differences within low-precipitation continental regions can also be considerable. This is particularly the case for the Sahel region of northern Africa and the Antarctic continental interior (Fig. S2). We hypothesise that GCMs applied to

CPD
11, 3277–3339, 2015

the study of paleoclimates are also likely to show significant regional differences in their precipitation distribution, underlining the importance of model intercomparison. Figure 2 additionally shows that all of the EoMIP models simulate a global precipitation rate which agrees fairly well with observational data sets for preindustrial climatology (CMAP, GPCP, Legates and Willmott, 1990). Given that all of the models simulate the principal features of MAP distribution, we carry all forward to our Eocene analysis.

3.2 Sensitivity of the global Eocene hydrological cycle to greenhouse gas forcing

The EoMIP model simulations were configured with a range of plausible early Eocene and PETM atmospheric CO_2 levels, yielding a range of global mean surface air temperatures (Lunt et al., 2012). It is therefore possible to evaluate how consistently precipitation rates are simulated across the GCMs (i) for a given CO_2, (ii) for a given global mean temperature, or in the case of those models for which multiple simulations have been performed, (iii) for a given CO_2 change and (iv) for a given global mean temperature change. Closure of the GCM global hydrological budget requires that total annual precipitation and evaporation are equal, providing there is no net change in water storage – the imbalances, summarised in Table S1 are $< 0.01\,\mathrm{mm\,day^{-1}}$ equivalent. In HadCM3L, the interannual range in global annual mean precipitation rate across the 95 years over which mean climatology is averaged is 0.07 and $0.06\,\mathrm{mm\,day^{-1}}$ in the ×2 and ×6 CO_2 simulations, respectively, such that the maximum global annual precipitation rate in the timeseries is less than 2.5 % above the minimum rate. We therefore consider mean annual precipitation rate to be a robust estimate of the overall sensitivity of the simulated hydrological cycle. Precipitation rates calculated from three modern observational datasets are shown in Fig. 2b (open circles) and are in relatively good agreement with the rates derived from preindustrial simulations (filled circles), providing confidence in this measure.

CPD
11, 3277–3339, 2015

All of the EoMIP models exhibit a more intense hydrological cycle for the Eocene (Fig. 2b; squares) compared to that simulated in the corresponding preindustrial simulations (Fig. 2b; circles). For a given CO_2, the models vary in the intensity of the hydrological cycle they simulate – for example, ECHAM5 has a global precipitation rate at 2 × preindustrial CO_2 comparable to that of CCSM3_W at ∼ 12 × preindustrial CO_2. In the remainder of this section, we discuss reasons for these differences, which can be attributed to (i) differences in global/regional temperatures between the simulations, (ii) differences in Eocene boundary conditions, (iii) variation of poorly constrained parameter values and (iv) more fundamental differences in the ways in which the models simulate hydrology.

The GCMs within the EoMIP ensemble differ in their global mean temperature for a given CO_2 (e.g. Lunt et al., 2012; Fig. 2a). Consequently, the global precipitation rate for each ensemble member is shown in Fig. 2c relative to its globally averaged surface air temperature. This demonstrates that much of the variation between models in precipitation rate arises from these temperature differences. For example, the elevated precipitation rate in the 2 × CO_2 ECHAM5 is explained by this model's warmth, being globally > 5 °C warmer than HadCM3L at the same CO_2. Similarly, the enhanced precipitation rate in the CCSM3_K simulations at both ∼ ×5 CO_2 and ∼ ×9 CO_2 relative to those simulated in CCSM3_H and CCSM3_W are attributable to warmer surface temperatures in CCSM3_K, resulting from alterations to cloud condensation nuclei (CNN) parameters, with a reduction in low-level cloud acting to increase short-wave heating at the surface (Kiehl and Shields, 2013). The reduced aerosol loading in CCSM3_H results in surface warming relative to CCSM3_W (Fig. 2a), which explains much of the 7–8 % increase in strength of the hydrological cycle across the CO_2 range studied; the ×4 CO_2 simulation in CCSM3_W has approximately the same surface temperature as CCSM3_H at ×2 CO_2. There are effects beyond those induced by surface temperature, however. For example, for a given surface air temperature, the global precipitation rate is consistently weaker in CCSM_W relative to CCSM_H (Fig. 2c) – possibly a re-

CPD
11, 3277–3339, 2015

sult of modified aerosol-cloud interactions due to the changes in prescribed aerosols in CCSM_H.

The degree to which the global hydrological cycle will intensify with future global warming has received much attention (e.g. Allen and Ingram, 2002; Held and Soden, 2006; Trenberth, 2011). Held and Soden (2006) show a ~ 2 % increase in global precipitation per degree of warming for AR4 GCMs forced with the A1B emissions scenario, but with notable inter-model variability. For those simulations with multiple CO_2 forcing, it is possible to estimate how this sensitivity varies for the Eocene. We show the dP/dT relationships for each model as well as the increase in % precipitation for a 1 °C temperature increase over the range of 15–30 °C (Table 2). Both CCSM3 and HadCM3L appear to be broadly comparable at ~ 1.8–2.1 % increase in the intensity of the hydrological cycle for each degree of warming, consistent with the future climate simulations.

Some variation in the intensity of the hydrological cycle simulated by the EoMIP models may be expected to occur independently of global mean surface air temperature. For preindustrial conditions, boundary conditions are largely constant (atmospheric composition, continental positions, orography and ice sheet distribution), yet the simulations show a spread of ~ 0.30 mm day^{-1} – which exceeds the precipitation increase for a doubling of CO_2 from ×2 to ×4 preindustrial in both CCSM3_H (0.13 mm day^{-1}) and HadCM3L (0.18 mm day^{-1}) – these differences are not explained by differences in preindustrial temperature (Fig. 2b) but may relate to more fundamental differences in model physics, particularly between HadCM3L and CCSM3W, where a more active hydrological cycle is consistently simulated in HadCM3L for both the Eocene and preindustrial conditions.

For both the ×2 and ×4 CO_2 simulations, the HadCM3L simulations that include the TRIFFID dynamic vegetation model have a near identical precipitation rate to those without (Fig. 2b). However, the ×4 CO_2 simulation with dynamic vegetation is substantially warmer than the ×4 simulation with fixed homogenous shrubland. The inclusion of the dynamic vegetation model acts to warm the surface climate as described in Loptson

CPD
11, 3277–3339, 2015

et al. (2014), but this does not yield an associated increase in precipitation. This may be related to the fact that temperature differences induced by TRIFFID are concentrated over the land surface, where the evapotranspiration rate is limited by moisture availability. The TRIFFID simulations therefore exhibit a reduced hydrological sensitivity of $\sim 1.3\,\%$ increase in precipitation per degree of warming (dP/dT) compared with $\sim 1.8\,\%$ for the non-TRIFFID simulations.

In the FAMOUS simulations undertaken by Sagoo et al. (2013; Fig. 2d), all simulations are performed at $2 \times CO_2$, but global temperatures range between 12.3 and 31.8 °C on account of simultaneous variation of 10 uncertain parameter values, some of which directly influence cloud formation and precipitation. Within these simulations there is also a linear relationship between surface air temperature and global precipitation ($R^2 = 0.965$; $n = 17$) suggesting the global intensity of the hydrological cycle remains primarily coupled to global temperature, despite greater scatter around the dP/dT relationship. Despite this, the overall dP/dT relationship in FAMOUS is higher than that of HadCM3L and HadCM3L + TRIFFID, with an $\sim 2.8\,\%$ increase in precipitation for each degree of warming (Table 2).

In HadCM3L, the $1 \times CO_2$ Eocene and preindustrial simulations have similar global precipitation rates (Fig. 2a), implying that Eocene boundary conditions other than CO_2 do not exert a major influence on the intensity of the hydrological cycle, raising global precipitation rate by only $\sim 0.10\,\mathrm{mm\,day^{-1}}$. However, this increase is consistent with and likely driven by a small increase in global surface air temperature. Furthermore, the preindustrial simulations for both CCSM3 and HadCM3L lie on, or close to, the Eocene-derived dP/dT lines (Fig. 2c), suggesting that globally, precipitation rate for a given temperature is not increased/decreased for the Eocene, despite differences in low-latitude land–sea distribution, ocean gateways and a lack of Eocene ice sheets.

Intriguingly, extrapolating the dP/dCO_2 relationship backwards to $1 \times CO_2$ for CCSM_W would require an Eocene precipitation rate $\sim 7\,\%$ above that of the preindustrial rate. This suggests a more substantial effect of Eocene boundary conditions on elevating absolute precipitation rates for CCSM3_W than that seen in HadCM3L, but

CPD
11, 3277–3339, 2015

still operating via temperature effects. GISS-ER has a marginally more vigorous hydrological cycle than the other models for a given global temperature. Roberts et al. (2009) show that the global precipitation rate in a preindustrial $4 \times CO_2$ simulation in GISS-ER is $\sim 4\,\%$ greater than that of the preindustrial, whereas the Paleogene simulation has a precipitation rate $\sim 23\,\%$ above that of the preindustrial. Therefore Paleogene boundary conditions other than CO_2 are crucial in elevating precipitation rate in this model.

3.3 Variability in Mean Annual Precipitation (MAP) distribution

3.3.1 Spatial distribution of MAP

Figure 3 shows MAP distributions for each EoMIP simulation. Eocene distributions are relatively similar to those for preindustrial conditions (Fig. 1), with clearly recognisable inter-tropical convergence zone (ITCZ), South Pacific convergence zone (SPCZ) and subtropical precipitation minima, the distributions of which appear to be long-standing characteristics of Cenozoic precipitation. Relative to preindustrial simulations, the Eocene distributions exhibit increased precipitation at high latitudes as a consequence of elevated Eocene temperatures in these regions. In CCSM in particular, the Eocene is characterised by a more globally equable precipitation rate: the expansion of zones of highest precipitation in the Eocene relative to preindustrial is muted compared with a more extensive loss of low precipitation regions. Additional support for this is provided by a comparison of mean precipitation rates for land and ocean (Table S2). The preindustrial ratio of land : ocean precipitation is maintained in the Eocene HadCM3L and ECHAM simulations, whereas in CCSM, precipitation rates over land and ocean are typically equal. The effects of differences in simulated surface air temperatures between models within the ensemble are also evident: for a given global surface temperature, HadCM3L maintains cooler poles than CCSM3 and ECHAM5 (Sect. 3.3.2) and regions with MAP $< 300\,\mathrm{cm\,year^{-1}}$ persist in the Arctic and Antarctic even at $\times 4$ CO_2.

CPD
11, 3277–3339, 2015

Modelled Eocene MAP features are frequently traceable to those identified in preindustrial simulations (Sect. 3.1), including the single tropical convergence zone in the GISS ×4 CO_2 simulation and the double ITCZ in a number of the models. Elsewhere, the Eocene precipitation distributions diverge from those of the preindustrial simulations and may be related to specific Eocene paleogeography, elevated CO_2, or other boundary conditions. In HadCM3L, there is a clear trend towards a more south-easterly trending SPCZ in the higher CO_2 simulations, which is not replicated in the warm simulations of the sister model FAMOUS. The SPCZ in CCSM is also far weaker in the Eocene simulations, compared to preindustrial simulations. Despite similar preindustrial precipitation distributions over tropical Africa, CCSM and HadCM3L strongly diverge in the Eocene, with CCSM showing far more intense equatorial precipitation. The FAMOUS simulations E16 and E17 represent two realisations of very warm climates with a reduced equator-pole temperature gradient – in these simulations significant increases in mid-latitude precipitation are particularly accentuated over the Pacific Ocean; increases in convection in the subtropics and mid-latitudes are sufficient to eliminate the precipitation minima seen in other models at these latitudes.

For a given CO_2, differing boundary conditions and simulated model air temperatures prevent direct assessment of whether Eocene regional precipitation distributions are robust to GCM selection. We show a multimodel mean in Fig. 5 for simulations with a common global precipitation rate. Elevated high-latitude precipitation for the early Eocene relative to preindustrial conditions is robust between GCMs, although absolute values remain variable between models, particularly in the Southern Hemisphere likely due to differing Antarctic orography. Differences between models in the mid-latitudes are smaller, resulting in some confidence that the secondary precipitation maxima were polewards of their preindustrial location during the Eocene. Equatorial precipitation remains highly variable between models but is accentuated relative to preindustrial.

CPD
11, 3277–3339, 2015

3.3.2 Controls on precipitation distribution

Precipitation rates for each simulation are summarised in Table S2, including separate rates calculated over land and ocean surfaces and rates deconvolved into those arising from convective and large-scale contributions. These data show that elevated precipitation rates in the high CO_2 Eocene simulations are largely the result of increased convection, although in the ECHAM5 model a greater percentage of precipitation is generated by large scale mechanisms in both the Eocene and preindustrial simulation. Figure 4 shows how convective and large-scale precipitation rates vary with latitude for a selection of the EoMIP simulations. This reveals differences between models in the mechanisms responsible for precipitation distributions which can be related to surface air temperature distributions. In the HadCM3L simulations, the mid-latitude maxima in both large scale and convective precipitation advance polewards with increasing CO_2 with precipitation increases over the high northern latitudes driven almost exclusively by enhanced large-scale precipitation. CCSM3 has substantially warmer poles which results in much enhanced high-latitude large scale precipitation relative to HadCM3L, although large scale latitudinal contributions differ somewhat for preindustrial simulations at both low and high latitudes. In CCSM3_K, the warmest CCSM3 simulations, polar temperatures are elevated compared to CCSM3_H as is total precipitation in these regions, but in this case large scale precipitation is reduced over much of the high latitudes and the higher total precipitation is due to convective processes.

In the warmest FAMOUS simulations of Sagoo et al. (2013), the high latitudes experience particularly significant increases in large scale precipitation, such that the maximum values are those at the poles in the E17 simulation, and in the Southern Hemisphere the local mid-latitude precipitation maximum is lost. Elevated mid latitude temperatures in the warm FAMOUS simulations additionally result in significant increases in convective precipitation which are not simulated in the cooler simulations and models. Overall, convective precipitation in FAMOUS increases as both global temperatures rise and equatorial-to-polar temperature gradients decrease, regardless

CPD
11, 3277–3339, 2015

of the underlying parameter configuration; this emphasises the fundamental control of temperature distribution on precipitation, as opposed to the effect of alteration of any one specific parameter.

For HadCM3L and CCSM3, simulations at different CO_2 provide an insight into how regional Eocene precipitation distributions are impacted by warming, and anomaly plots for high – low CO_2 simulations are shown in Fig. 6. For the same CO_2 forcing, CCSM3 is globally cooler than HadCM3L (Lunt et al., 2012), but the anomalies for 16 – 4 CO_2 (CCSM_W) and 6 – 2 CO_2 (HadCM3L) display similar global changes in both temperature and therefore precitation rate on account of similar dP/dT relationships (Fig. 2; Table 2). Intriguingly, HadCM3L displays far greater spatial contrasts in net precipitation change, particularly over the ocean: between the pair of HadCM3L simulations, some 23 % of the Earth's surface experiences an increase or decrease in precipitation greater than 60 cm year^{-1}, compared to just 6 % in the CCSM3 simulations. Some spatial patterns are robust between models – including the dipole-like pattern over the Pacific, SPCZ migration, and subtropical reductions in precipitation at the expense of greater moisture transport to higher latitudes. Other changes are model dependent: in HadCM3L, there is a clear increase in the strength of storm tracks along the eastern Asian coastline, which is not repeated in CCSM. In HadCM3L, additional decreases in precipitation occur around the Peri-Tethys and along the coastline of equatorial Africa. Whilst models within the EoMIP ensemble therefore show similarities in their global rate of precipitation change with respect to temperature, regional precipitation distributions are strongly model dependent, diverging within the EoMIP ensemble according to surface air temperature characteristics.

3.4 Precipitation seasonality

The evolution and timing of the onset of global monsoon systems in the Eocene has been the subject of debate (Licht et al., 2014; Sun and Wang, 2005; Wang et al., 2013). Proxy studies for the early Eocene have highlighted differences in precipitation seasonality relative to modern (Greenwood et al., 2010; Greenwood, 1996; Schubert

CPD
11, 3277–3339, 2015

et al., 2012) and possible changes to seasonality at the PETM have also been invoked in a number of studies (Sluijs et al., 2011; Schmitz and Pujalte, 2007; Handley et al., 2012). Previous modelling work utilising CCSM3 has suggested that much of the mid-late Eocene was monsoonal, with up to 70 % of annual rainfall occurring during one extended season in North and South Africa, North and South America, Australia and Indo-Asia (Huber and Goldner, 2012). GCMs have been shown to differ greatly in their prediction of future monsoon systems (e.g. Turner and Slingo, 2009; Chen and Bordoni, 2014) so we examine the similarities and differences in Eocene models with respect to the seasonality of their precipitation distributions.

Figure 7 shows the percentage of precipitation falling in the extended summer season (MJJAS for Northern Hemisphere; NDJFM for Southern Hemisphere) following the approach of Zhang and Wang (2008) and also utilised in the Eocene studies of Huber and Goldner (2012) and Licht et al. (2014). This metric has been shown to correlate well with the modern-day distribution of monsoon systems. Overall, the models show a global distribution of early Eocene monsoons in high CO_2 climates that is similar to those simulated under preindustrial simulations (Fig. S6). Australia is markedly less monsoonal than in preindustrial simulations due to its more southerly Eocene paleolocation. Note that regions where winter season precipitation dominates fall at the lower end of the scale; these tend to be over the ocean surface but also include regions around the Peri-Tethys and both the Pacific and Atlantic US coasts.

HadCM3L is notable in that it is more seasonal at high latitudes, simulating an early Eocene monsoon centred over modern day Wilkes' Land region of Antarctica. Although proxy data have suggested highly seasonal precipitation regimes for both the Arctic (Schubert et al., 2012) and Antarctic (Jacques et al., 2014) during this interval, these systems are maximised in the ×2 CO_2 simulation and weaken somewhat in the simulations with elevated CO_2. This arises due to the high temperature seasonality of Arctic/Antarctic Eocene regions in HadCM3L relative to the other models (e.g., Gasson et al., 2013). In austral winter, Antarctic temperatures are sufficiently low to suppress precipitation, although this constraint is lifted somewhat in the higher CO_2 simulations

CPD
11, 3277–3339, 2015

which produce more equable rainfall. The effect of elevated global warmth on the extent of Eocene monsoons is additionally consistent across the models, with a decline in terrestrial areas with seasonal precipitation regimes at higher CO_2 simulations (Table 3). HadCM3L simulates a 6 % reduction in the extent of terrestrial regions influenced by monsoonal regimes for HadCM3L ×1 CO_2 relative to the preindustrial simulation, which appears to be related to the warmer surface temperatures and absence of Antarctic ice sheet.

3.5 $P - E$ distributions

The difference between precipitation and evaporation ($P - E$) is important to consider in the characterisation of an enhanced Eocene hydrological cycle. Over land, this parameter broadly determines the precipitation available to become soil water and surface runoff, the partitioning itself being dependent on the land surface schemes within the models (e.g. Cox et al., 1998; Oleson et al., 2004). Over the ocean, $P - E$ drives differences in salinity which can affect the Eocene ocean circulation (Bice and Marotzke, 2001; Waddell and Moore, 2008). We show mean annual ($P - E$) budgets for each of the EoMIP simulations in Fig. 8. In warmer climates, an exacerbation of existing ($P - E$) is expected – that is, the wet become wetter and the dry drier, as the moisture fluxes associated with existing atmospheric circulations intensify (Held and Soden, 2006). Broadly, the EoMIP simulations support this paradigm for the Eocene relative to preindustrial (Fig. 5). CCSM3 shows fairly minor changes in the boundaries between net-precipitation and net-evaporation zones at higher CO_2 (Fig. 8), although the net-evaporation zones in HadCM3L do migrate polewards over the eastern Pacific and North Atlantic at high CO_2. Other dynamic changes within HadCM3L are coupled to the precipitation responses: the more meridionally-orientated SPCZ results in a weaker zonally averaged Southern Hemisphere evaporative zone (Fig. 9) and the expansion of precipitation along the Asian coastline results in a more positive ($P - E$) balance in this region. Over continents the models also display different responses. Over equatorial and northern Africa, HadCM3L simulates increasingly wet climates in the high CO_2

CPD
11, 3277–3339, 2015

simlations, driven by increases in precipitation coupled to reductions in evaporation. In CCSM3, the net moisture balance is less responsive with respect to temperature, although instense equatorial precipitation means this region is much wetter than in HadCM3L.

Because of the large latent heat fluxes involved in evaporation and condensation, the global hydrological cycle acts as a meridional transport of energy. Net evaporation in the subtropics stores energy in the atmosphere as latent heat, releasing it at high latitudes via precipitation (Pierrehumbert, 2002). An intensified hydrological cycle, associated with increased atmospheric transport of water vapour has therefore been suggested as a potential mechanism for reducing the equator-pole temperature gradient during greenhouse climates (Ulfnar et al., 2004; Caballero and Langen, 2005). By integrating the area-weighted estimates of $P - E$ with latitude, we show how these contributions differ between the EoMIP models and associated preindustrial simulations in Fig. 9. Relative to preindustrial climatology, the intensification of the hydrological cycle associated with increased drying in the net-evaporative zones and increased moistening of the net-precipitation zones implies a stronger latent heat flux and within the EoMIP ensemble, the implied polewards energy fluxes of the E16 and E17 FAMOUS simulations and $\times 2$ CO_2 ECHAM simulation are particularly significant. GISS-ER has a particularly strong low latitude equatorially-directed latent heat transfer which arises from the much elevated Eocene precipitation rate in the deep tropics. At face value, it may seem that the elevated latent heat transport at mid to high latitudes could contribute towards the reduced equator-pole temperature gradient in the EoMIP simulations, but we note that theoretical and modelling based studies suggest increased latent heat transport is associated with an increased equator-pole temperature gradient (Pagani et al., 2014). Within the EoMIP ensemble, meridional temperature gradients and global surface air temperatures covary and so it is not possible to separate clearly the effects of these different controls (Fig. S3). Nevertheless, these results illustrate that relative to preindustrial, the Eocene hydrological cycle acts as to elevate the meridional transport of latent heat, particularly around 45–50° N/S of the equator.

CPD
11, 3277–3339, 2015

4 Proxy-model comparison

A range of proxy data provide constraints on how the early Eocene hydrological cycle differed to that of the modern, including oxygen isotopes from mammalian, fish and foraminiferal fossils (Clementz and Sewall, 2011; Zachos et al., 2006; Zacke et al., 2009) and the distribution of climatically sensitive sediments (e.g. Huber and Goldner, 2012). Changes in regional hydrology at the PETM have also been inferred from geomorphological (John et al., 2008; Schmitz and Pujalte, 2007), biomarker (Handley et al., 2011; Pagani et al., 2006) and microfossil (Sluijs et al., 2011; Kender et al., 2012) proxies. These have often resulted in qualitative interpretations of hydrological change, although the climatic variables and temporal signal they proxies record are uncertain in many instances (e.g. Handley et al., 2011, 2012; Tipple et al., 2013; Sluijs et al., 2007). However, quantitative estimates of Mean Annual Precipitation (MAP), derived from micro- and macro-floral fossils have been made for a number of early Eocene and PETM-aged sections which can be compared directly with the GCM-estimated precipitation rates described in Sect. 3.

Paleoprecipitation estimates are primarily produced by two distinct paleobotanic methods – leaf physiogonomy and Nearest Living Relative (NLR) approaches. In the former, empirical univariate and multivariate relationships have been established between the size and shape of modern angiosperm leaves and the climate in which they grow, with smaller leaves predominating in low precipitation climates (e.g. Wolfe, 1993; Wilf et al., 1998; Royer et al., 2005). The NLR approach estimates paleoclimate by assuming fossilised specimens have the same climatic tolerances as their presumed extant relatives. This approach can utilise pollen, seeds and fruit in addition to leaf fossils (Mosbrugger et al., 2005). Relative to Mean Annual Temperature, geologic estimates of MAP are less precise, which may relate to decoupling between MAP and local water availability (Peppe et al., 2011; Royer et al., 2002), a greater importance of growing season (Mosbrugger and Utescher, 1997) or in the case of physiogonomical approaches, competing influence of other climatic variables (Royer et al., 2007).

CPD
11, 3277–3339, 2015

Our data compilation is provided in Table S3. Some of the data has been compared previously with precipitation rates from an atmosphere-only simulation performed with isoCAM3 for the Azolla interval (~ 49 Ma; Speelman et al., 2010). Our proxy-model comparison includes data for the remainder of the early-mid Eocene, including a number of recently-published estimates such that the geographic spread is widened to include estimates from Antarctica (Pross et al., 2012), Australia (Contreras et al., 2013; Greenwood et al., 2003), New Zealand (Pancost et al., 2013), South America (Wilf et al., 2005) and Europe (Eldrett et al., 2014; Mosbrugger et al., 2005; Geisental et al., 2011). We select Ypresian-aged data where multiple Eocene precpitation rates exist, including estimates for the PETM but have additionally included some Lutetian and Paleocene data, particularly in regions where Ypresian data does not exist. This approach is justified given the range of plausible Eocene CO_2 with which simulations have been performed.

Figure 10 shows paleobotanical estimates for MAP for a range of the data in Table S2, along with model-estimated rates for each of the EoMIP simulations. Mean precipitation estimates from each model are derived by averaging over grid boxes centred on the paleolocation in a similar approach to Speelman et al. (2010). This is a nine cell grid of 3×3 gridboxes for HadCM3L, GISS, ECHAM and CCSM3, although in some instances an eight cell grid of 2×4 is used along paleocoastlines. Differing model resolutions and land–sea masks result in averaging signals from slightly different paleogeographic areas, but this approach allows for an assessment of the regional signal and error bars are included to show the range of precipitation rates present within the locally defined grid. In the reduced resolution model, FAMOUS, mean and range are derived from 2×2 gridboxes to ensure regional climatologies remains comparable. Error bars on the geologic data are generally provided as described in the original publications, with further details also provided in Table S3.

Our results confirm different regional sensitivities across the models. Over New Zealand (Fig. 10b), HadCM3L shows a strong sensitivity to increases in CO_2, whereas in CCSM3, elevated CO_2 has little effect on precipitation rate. This can be interpreted

CPD
11, 3277–3339, 2015

in terms of the differing SPCZ precipitation structures, with HadCM3L simulating a shift of the rain-belt towards New Zealand in the warmer simulations (Fig. 6). Conversely, in the Western US (Fig. 10g), HadCM3L is stable with respect to increases in CO_2 whilst CCSM3 produces increases in preciptation in higher CO_2 simulations. Furthermore, significant variations occur between the degree of match the models show with proxy precipitation estimates. At grid boxes corresponding to modern day Axel Heiberg Island (Fig. 10h), HadCM3L and GISS-ER are unable to produce sufficient precipitation, whereas the high CO_2 CCSM3 and E16/17 FAMOUS simulations are in closer agreement. Over Wilkes Land, Antarctica, all of the EoMIP models show sensitivity to CO_2, but unanimously produce too little precipitation, although the FAMOUS and CCSM_K simulations with warmer polar temperatures (Fig. 4) come closest to replicating the central estimates of geologic data (although some caution is required in how these differencess are interpreted, given that preindustrial GCM errors are also typically of the order of 300 mm year^{-1} too little precipitation over this region). A similar pattern is apparent in the Paleocene North West Territory data (Fig. 10l), with the cooler pole models and those at low CO_2 showing a dry bias. At the mid latitudes, model biases relative to paleoprecipitation estimates are reduced, including for the continental US (Fig. 10f), Argentina (Fig. 10g) and central Europe (Fig. 10m), where proxy data are within the precipitation range simulated across the suite of simulations.

At Tanzania (Fig. 10e), all model simulations appear to overprecipitate and elevating CO_2 has relatively little impact on precipitation rate in a number of the models. In the HadCM3L simulations in particular, elevating CO_2 to levels required to produce a match with early Eocene high-latitude data results in over-precipitation at this site. With a scarcity of low latitude data, this interpretation remains tentative, particularly given that a number of the models show a marginal preindustrial wet bias over tropical Africa (Fig. 1) and leaf physiognomic methods tend to result in lower precipitation estimates than those provided by other proxies (e.g., Peppe et al., 2011). The more robust observation is that the models produce too little precipitation at locations corresponding to Eocene high latitude sites, and this is consistent with suggestions that GCMs

CPD
11, 3277–3339, 2015

fail to simulate high-latitude warmth for the Early Eocene. If high latitude temperatures are too cold in the model, then the saturation vapour pressure of the atmosphere is suppressed and polewards-moving airmasses lose moisture via rainout earlier in their trajectory. We demonstrate this coupling of data-model temperature and precipitation errors in Fig. 9. In HadCM3L, increasing CO_2 from ×2 to ×6 decreases temperature and precipitation anomalies at the majority of sites, resulting in better overall match to the geologic data. In the case of CCSM3, a relatively good match with precipitation proxy estimates is achieved at both low and high CO_2, but models appear too cold at low CO_2. In FAMOUS and CCSM3_K, parameter sets which reduce the equator-pole temperature gradient and warm the high latitudes are able to minimise errors in both temperature and precipitation with the majority of the geologic data at low CO_2. However, in FAMOUS, E17 simulates surface air temperatures > 45 °C in Colombia, which produces a significant temperature data-model anomaly.

Whilst our compilation allows for some degree of model intercomparison, it is far from a global data set, with a bias towards mid and high latitude sites, and a lack of data from low latitudes (Fig. S5). There is also a need for further proxy-model comparisons from high latitudes to corroborate our analysis. The paleobotanic estimates included here support the concept of a " fossil climate" at high latitudes – i.e. a paleoclimatic state with no modern analogue, which compromises the application of the Nearest Living Relative concept and leaf area analysis, especially given leaf size is thought to be a trade off between maximising photosynthesis and minimising water loss (Peppe et al., 2011). Furthermore, on a warm Earth, the potential for decoupling between precipitation rate and water availability may have been enhanced at the high latitudes, particularly if increased precipitation was offset by elevated evaporation. Since $P - E$ is typically > 0 over land surfaces (Greve et al., 2014), land aridity indices such as P/PET which describe the atmopsheric water demand relative to the land surface may also assist in understanding demands on plants in a high CO_2 world. The effect of a different Eocene seasonal cycle also requires further consideration. The models which are cooler at the poles such as HadCM3L show a stronger seasonal cycle in precipitation (Fig. 5)

CPD
11, 3277–3339, 2015

and growing season precipitation from these simulations may minimise the data-model anomaly we have described. Nonetheless, current best estimates of early and mid Eocene precipitation rate provide independent evidence for a proxy-model anomaly at high latitudes.

5 Conclusions

The simulations within the EoMIP ensemble support an intensified hydrological cycle for the early Eocene, characterised by enhanced global mean precipitation and evaporation rates and increased meridional latent heat transport. The sensitivity of Eocene precipitation rates to warming is within the range suggested for future IPCC-style climate change scenarios, although some variation is introduced by models which incorporate additional feedbacks such as the TRIFFID simulations of Loptson et al. (2014). Differences in Eocene surface temperature distributions drive differences between models in their regional precipitation rates including for models with similar global precipitation sensitivities (dP/dT). Anomalies between simulations at high and low CO_2 may provide a way by which to constrain changes in precipitation occurring during hyperthermals (Winguth et al., 2010). Regions which are particularly different between HadCM3L and CCSM3 include coastal regions around the Peri-Tethys, the South Pacific, and tropical Africa which may represent targets for future proxy-data acquisition. The modern-day distribution of monsoons appears largely similar to that of the early Eocene across the EoMIP ensemble and the presence of monsoons across a range of CO_2 corroborates the work of Huber and Goldner (2012). The results suggest a decline in the extent of monsoon-influenced terrestrial regions in high-CO_2, warm climates, which may have implications for the interpretation of proxy data from hyperthermal events, such as the PETM, and for understanding the long-term evolution of monsoon systems.

Our proxy comparison emphasises the coupling between temperature and precipitation data-model anomalies. For high latitude sites, model simulations are typically

CPD
11, 3277–3339, 2015

too cold, resulting in suppressed precipitation across a number of the models. Model simulations which enhance high-latitude warmth are in better agreement with existing proxy data, but the size of precipitation error bars prevents an identification of a "best" simulation. Models which warm the poles via high CO_2 (Liu et al., 2009; Winguth et al., 2010) are equally successful as models which achieve warmth at low CO_2 via varying poorly constrained parameter values (Sagoo et al., 2013; Kiehl and Shields, 2013). Better constraints on early Eocene CO_2 and more data from low latitudes are now required, as are other proxy approaches which can verify the high latitude anomaly we have observed. Forward proxy modelling of water isotopes (Speelman et al., 2010; Sturm et al., 2009; Tindall et al., 2010) and comparison to archives which incorporate an Eocene δD or $\delta^{18}O$ signal (Zacke et al., 2009; Krishnan et al., 2014; Fricke and Wing, 2004) represents one such avenue.

Proxies sensitive to hydrological changes offer an independent means to temperature by which to assess paleoclimatic model performance. Whilst elevated CO_2 causes a near-global increase in model-simulated surface temperatures, the same warming results in regions of both increased and reduced precipitation and $P - E$ within climate models. Even without tightly constrained absolute changes in precipitation or net hydrological balance the spatial pattern of qualitative indicators may therefore provide a critical test of GCM ability for warm paleoclimates. Where estimates of absolute precipitation rates do exist, our preliminary model-data comparison indicates that GCMs are broadly unable to simulate sufficient high-latitude precipitation for the early Eocene, even with CO_2 configured at the upper end of proxy inferred estimates. Precipitation biases within models are coupled to those of temperature and our analysis is therefore consistent with the prevailing view of enhanced early Eocene high latitude warmth. Our study represents a first step towards characterising the variability of the Eocene hydrological cycle simulated in GCMs. Further work is now required to study how other modelled aspects of the hydrological cycle such as runoff and salinity vary within the Eocene, and how these hydrological changes may relate to signals preserved in the geological record.

CPD
11, 3277–3339, 2015

The Supplement related to this article is available online at doi:10.5194/cpd-11-3277-2015-supplement.

References

Abbot, D. S. and Tziperman, E.: A high-latitude convective cloud feedback and equable climates, Q. J. Roy. Meteor. Soc., 134, 165–185, doi:10.1002/qj.211, 2008.

Akkiraz, M. S., Kayseri, M. S., and Akgun, F.: Palaeoecology of coal-bearing Eocene sediments in Central Anatolia (Turkey) based on quantitative palynological data, Turk. J. Earth Sci., 17, 317–360, 2008.

Allen, M. R. and Ingram, W. J.: Constraints on future changes in climate and the hydrologic cycle, Nature, 419, 224–232, doi:10.1038/nature01092, 2002.

Beerling, D. J., Fox, A., Stevenson, D. S., and Valdes, P. J.: Enhanced chemistry-climate feedbacks in past greenhouse worlds, P. Natl. Acad. Sci. USA, 108, 9770–9775, doi:10.1073/pnas.1102409108, 2011.

Bice, K. L. and Marotzke, J.: Numerical evidence against reversed thermohaline circulation in the warm Paleocene/Eocene ocean, J. Geophys. Res.-Oceans, 106, 11529–11542, doi:10.1029/2000jc000561, 2001.

Bijl, P. K., Schouten, S., Sluijs, A., Reichart, G. J., Zachos, J. C., and Brinkhuis, H.: Early Palaeogene temperature evolution of the southwest Pacific Ocean, Nature, 461, 776–779, doi:10.1038/Nature08399, 2009.

Bolle, M. P. and Adatte, T.: Palaeocene early Eocene climatic evolution in the Tethyan realm: clay mineral evidence, Clay Miner., 36, 249–261, doi:10.1180/000985501750177979, 2001.

Bolle, M. P., Pardo, A., Adatte, T., Tantawy, A. A., Hinrichs, K. U., Von Salis, K., and Burns, S.: Climatic evolution on the southern and northern margins of the Tethys from the Paleocene to the early Eocene, GFF, 122, 31–32, doi:10.1080/11035890001221031, 2000.

Bowen, G. J., Beerling, D. J., Koch, P. L., Zachos, J. C., and Quattlebaum, T.: A humid climate state during the Palaeocene/Eocene thermal maximum, Nature, 432, 495–499, doi:10.1038/Nature03115, 2004.

Braconnot, P., Harrison, S. P., Kageyama, M., Bartlein, P. J., Masson-Delmotte, V., Abe-Ouchi, A., Otto-Bliesner, B., and Zhao, Y.: Evaluation of climate models using palaeoclimatic data, Nature Climate Change, 2, 417–424, doi:10.1038/nclimate1456, 2012.

CPD
11, 3277–3339, 2015

Chen, J. and Bordoni, S.: Intermodel spread of East Asian summer monsoon simulations in CMIP5, Geophys. Res. Lett., 41, 1314–1321, doi:10.1002/2013GL058981, 2014.

Clementz, M. T. and Sewall, J. O.: Latitudinal gradients in greenhouse seawater δ^{18}O: evidence from Eocene sirenian tooth enamel, Science, 332, 455–458, doi:10.1126/science.1201182, 2011.

Collins, W. D., Bitz, C. M., Blackmon, M. L., Bonan, G. B., Bretherton, C. S., Carton, J. A., Chang, P., Doney, S. C., Hack, J. J., Henderson, T. B., Kiehl, J. T., Large, W. G., McKenna, D.S ., Santer, B. D., and Smith, R. D.: The Community Climate System Model version 3 (CCSM3), J. Climate, 19, 2122–2143, doi:10.1175/JCLI-D-11-00290.1, 2006.

Contreras, L., Pross, J., Bijl, P. K., Koutsodendris, A., Raine, J. I., van de Schootbrugge, B., and Brinkhuis, H.: Early to Middle Eocene vegetation dynamics at the Wilkes Land Margin (Antarctica), Rev. Palaeobot. Palyno., 197, 119–142, doi:10.1016/j.revpalbo.2013.05.009, 2013.

Cox, P. M.: Description of the " TRIFFID " Dynamic Global Vegetation Model, Hadley Centre Technical Note, 24, 1–17, available at: http://www.metoffice.gov.uk/media/pdf/9/h/HCTN_24.pdf (last access: 16 July 2015), 2001.

Cox, P. M., Huntingford, C., and Harding, R. J.: A canopy conductance and photosynthesis model for use in a GCM land surface scheme, J. Hydrol., 212–213, 79–94, doi:10.1016/S0022-1694(98)00203-0, 1998.

Cox, P. M., Betts, R. A., Jones, C. D., Spall, S. A., and Totterdell, I. J.: Acceleration of global warming due to carbon-cycle feedbacks in a coupled climate model, Nature, 408, 184–187, doi:10.1038/35041539, 2000.

Dai, A.: Precipitation characteristics in eighteen coupled climate models, J. Climate, 19, 4605–4630, doi:10.1175/Jcli3884.1, 2006.

Douglas, P. M. J., Affek, H. P., Ivany, L. C., Houben, A. J. P., Sijp, W. P., Sluijs, A., Schouten, S., and Pagani, M.: Pronounced zonal heterogeneity in Eocene southern high-latitude sea surface temperatures, P. Natl. Acad. Sci. USA, 111, 6582–6587, doi:10.1073/pnas.1321441111, 2014.

Dunkley Jones, T., Lunt, D. J., Schmidt, D. N., Ridgwell, A., Sluijs, A., Valdes, P. J., and Maslin, M.: Climate model and proxy data constraints on ocean warming across the Paleocene–Eocene Thermal Maximum, Earth-Sci. Rev., 125, 123–145, doi:10.1016/j.earscirev.2013.07.004, 2013.

CPD
11, 3277–3339, 2015

Eberle, J. J.: A new "tapir" from Ellesmere Island, Arctic Canada – implications for northern high latitude palaeobiogeography and tapir palaeobiology, Palaeogeogr. Palaeocl., 227, 311–322, doi:10.1016/j.palaeo.2005.06.008, 2005.
Eberle, J. J. and Greenwood, D. R.: Life at the top of the greenhouse Eocene world – a review of the Eocene flora and vertebrate fauna from Canada's High Arctic, Geol. Soc. Am. Bull., 124, 3–23, doi:10.1130/B30571.1, 2012.
Eldrett, J. S., Greenwood, D. R., Harding, I. C., and Huber, M.: Increased seasonality through the Eocene to Oligocene transition in northern high latitudes, Nature, 459, 969–973, doi:10.1038/nature08069, 2009.
Eldrett, J. S., Greenwood, D. R., Polling, M., Brinkhuis, H., and Sluijs, A.: A seasonality trigger for carbon injection at the Paleocene–Eocene Thermal Maximum, Clim. Past, 10, 759–769, doi:10.5194/cp-10-759-2014, 2014.
Frakes, L. A.: Climates Throughout Geologic Time, Elsevier Scientific, Amsterdam, 310 pp.,1979.
Francis, J. E., Ashworth, A., Cantrill, D. J., Crame, J. A., Howe, J., Stephens, R., Tosolini, A.-M., and Thorn, V.: 100 million years of Antarctic climate evolution: evidence from fossil plants, in: Antarctica: a Keystone in a Changing World, Proceedings of the 10th International Symposium on Antarctic Earth Sciences, edited by: Cooper, A. K., Barrett, P. J., Stagg, H., Storey, E., Stump, E., Wise, W. and the 10th ISAES editorial team, The National Academies Press, Washington, DC, doi:10.3133/of2007-1047.kp03, 19–27, 2008.
Fricke, H. C. and Wing, S. L.: Oxygen isotope and paleobotanical estimates of temperature and δ^{18}O-latitude gradients over North America during the Early Eocene, Am. J. Sci., 304, 612–635, doi:10.2475/ajs.304.7.612, 2004.
Gayó, E., Hinojosa, L. F., and Villagrán, C.: On the persistence of Tropical Paleofloras in central Chile during the Early Eocene, Rev. Palaeobot. Palyno., 137, 41–50, doi:10.1016/j.revpalbo.2005.09.001, 2005.
Golovneva, L. B.: Early Palaeogene floras of Spitsbergen and North Atlantic floristic exchange, Acta Universitatis Carolinae – Geologica, 44, 39–50, 2000.
Greenwood, D. R.: Eocene monsoon forests in central Australia?, Aust. Syst. Bot., 9, 95–112, doi:10.1071/Sb9960095, 1996.
Greenwood, D. R., Moss, P. T., Rowett, A. I., Vadala, A. J., and Keefe, R. L.: Plant communities and climate change in southeastern Australia during the early Paleogene, in: Causes and

CPD
11, 3277–3339, 2015

Consequences of Globally Warm Climates in the Early Paleogene, The Geological Society of America, Inc., Boulder, CO., doi:10.1130/0-8137-2369-8.365, 365–380, 2003.
Greenwood, D. R., Archibald, S. B., Mathewes, R. W., and Moss, P. T.: Fossil biotas from the Okanagan Highlands, southern British Columbia and northeastern Washington State: climates and ecosystems across an Eocene landscape, Can. J. Earth Sci., 42, 167–185, doi:10.1139/e04-100, 2005.
Greenwood, D. R., Basinger, J. F., and Smith, R. Y.: How wet was the Arctic Eocene rain forest? Estimates of precipitation from Paleogene Arctic macrofloras, Geology, 38, 15–18, doi:10.1130/G30218.1, 2010.
Grein, M., Utescher, T., Wilde, V., and Roth-Nebelsick, A.: Reconstruction of the middle Eocene climate of Messel using palaeobotanical data, Neues Jahrb. Geol. P.-A., 260, 305–318, 2011.
Greve, P., Orlowsky, B., Mueller, B., Sheffield, J., Reichstein, M., and Seneviratne, S. I.: Global assessment of trends in wetting and drying over land, Nat. Geosci., 7, 716–721, doi:10.1038/ngeo2247, 2014.
Gruber, A., Su, X. J., Kanamitsu, M., and Schemm, J.: The comparison of two merged rain gauge-satellite precipitation datasets, B. Am. Meteorol. Soc., 81, 2631–2644, doi:10.1175/1520-0477(2000)081<2631:Tcotmr>2.3.Co;2, 2000.
Hack, J. J., Caron, J. M., Yeager, S. G., Oleson, K. W., Holland, M. M., Truesdale, J. E., and Rasch, P. J.: Simulation of the global hydrological cycle in the CCSM Community Atmosphere Model version 3 (CAM3): mean features, J. Climate, 19, 2199–2221, doi:10.1175/JCLI3755.1, 2006.
Hagemann, S., Arpe, K., and Roeckner, E.: Evaluation of the hydrological cycle in the ECHAM5 model, J. Climate, 19, 3810–3827, doi:10.1175/JCLI3831.1, 2006.
Handley, L., Pearson, P. N., McMillan, I. K., and Pancost, R. D.: Large terrestrial and marine carbon and hydrogen isotope excursions in a new Paleocene/Eocene boundary section from Tanzania, Earth Planet. Sc. Lett., 275, 17–25, doi:10.1016/j.epsl.2008.07.030, 2008.
Handley, L., Crouch, E. M., and Pancost, R. D.: A New Zealand record of sea level rise and environmental change during the Paleocene–Eocene Thermal Maximum, Palaeogeogr. Palaeocl., 305, 185–200, doi:10.1016/j.palaeo.2011.03.001, 2011.
Handley, L., O'Halloran, A., Pearson, P. N., Hawkins, E., Nicholas, C. J., Schouten, S., McMillan, I. K., and Pancost, R. D.: Changes in the hydrological cycle in tropical East Africa

CPD
11, 3277–3339, 2015

during the Paleocene–Eocene Thermal Maximum, Palaeogeogr. Palaeocl., 329, 10–21, doi:10.1016/j.palaeo.2012.02.002, 2012.
Heinemann, M., Jungclaus, J. H., and Marotzke, J.: Warm Paleocene/Eocene climate as simulated in ECHAM5/MPI-OM, Clim. Past, 5, 785–802, doi:10.5194/cp-5-785-2009, 2009.
Held, I. M. and Soden, B. J.: Robust responses of the hydrological cycle to global warming, J. Climate, 19, 5686–5699, doi:10.1175/JCLI3990.1, 2006.
Hinojosa, L. F. and Villagrán, C.: Did South American Mixed Paleofloras evolve under thermal equability or in the absence of an effective Andean barrier during the Cenozoic?, Palaeogeogr. Palaeocl., 217, 1–23, doi:10.1016/j.palaeo.2004.11.013, 2005.
Hinojosa, L. F., Pesce, O., Yabe, A., Uemura, K., and Nishida, H.: physiognomical analysis and paleoclimate of the Ligorio Márquez fossil flora, Ligorio Márquez formation, 46°45′ S, Chile, in: Post-Cretaceous Floristic Changes in Southern Patagonia, Chile, edited by: Nishida, H., ChuoUniv., Tokyo, 45–55, 2006.
Hollis, C. J., Taylor, K. W. R., Handley, L., Pancost, R. D., Huber, M., Creech, J. B., Hines, B. R., Crouch, E. M., Morgans, H. E. G., Crampton, J. S., Gibbs, S., Pearson, P. N., and Zachos, J. C.: Early Paleogene temperature history of the Southwest Pacific Ocean: reconciling proxies and models, Earth Planet. Sc. Lett., 349, 53–66, doi:10.1016/j.epsl.2012.06.024, 2012.
Huber, M.: Climate change. A hotter greenhouse?, Science, 321, 353–354, doi:10.1126/science.1161170, 2008.
Huber, M. and Caballero, R.: The early Eocene equable climate problem revisited, Clim. Past, 7, 603–633, doi:10.5194/cp-7-603-2011, 2011.
Huber, M. and Goldner, A.: Eocene monsoons, J. Asian Earth Sci., 44, 3–23, doi:10.1016/j.jseaes.2011.09.014, 2012.
Huber, M. and Sloan, L. C.: Heat transport, deep waters, and thermal gradients: coupled simulation of an Eocene greenhouse climate, Geophys. Res. Lett., 28, 3481–3484, doi:10.1029/2001GL012943, 2001.
Hunt, R. J. and Poole, I.: Paleogene West Antarctic climate and vegetation history in light of new data from King George Island, Geol. S. Am. S., 369, 395–412, doi:10.1130/0-8137-2369-8.395, 2003.
Jacobs, B. F. and Herendeen, P. S.: Eocene dry climate and woodland vegetation in tropical Africa reconstructed from fossil leaves from northern Tanzania, Palaeogeogr. Palaeocl., 213, 115–123, doi:10.1016/j.palaeo.2004.07.007, 2004.

CPD
11, 3277–3339, 2015

Jacques, F. M. B., Shi, G., Li, H., and Wang, W.: An early-middle Eocene Antarctic summer monsoon: evidence of "fossil climates", Gondwana Res., 25, 1422–1428, doi:10.1016/j.gr.2012.08.007, 2014.

John, C. M., Bohaty, S. M., Zachos, J. C., Sluijs, A., Gibbs, S., Brinkhuis, H., and Bralower, T. J.: North American continental margin records of the Paleocene–Eocene thermal maximum: implications for global carbon and hydrological cycling, Paleoceanography, 23, Pa2217, doi:10.1029/2007pa001465, 2008.

John, C. M., Banerjee, N. R., Longstaffe, F. J., Sica, C., Law, K. R., and Zachos, J. C.: Clay assemblage and oxygen isotopic constraints on the weathering response to the Paleocene–Eocene thermal maximum, east coast of North America, Geology, 40, 591–594, doi:10.1130/G32785.1, 2012.

Jones, C., Gregory, J., Thorpe, R., Cox, P., Murphy, J., Sexton, D., and Valdes, P.: Systematic optimisation and climate simulation of FAMOUS, a fast version of HadCM3, Clim. Dynam., 25, 189–204, doi:10.1007/s00382-005-0027-2, 2005.

Kaiser, T. M., Ansorge, J., Arratia, G., Bullwinkel, V., Gunnell, G. F., Herendeen, P. S., Jacobs, B., Mingram, J., Msuya, C., Musolff, A., Naumann, R., Schulz, E., and Wilke, V.: The maar lake of Mahenge (Tanzania) – unique evidence of Eocene terrestrial environments in sub-Sahara Africa, Z. Dtsch. Ges. Geowiss., 157, 411–413, 2006.

Kender, S., Stephenson, M. H., Riding, J. B., Leng, M. J., Knox, R. W. O. B., Peck, V. L., Kendrick, C. P., Ellis, M. A., Vane, C. H., and Jamieson, R.: Marine and terrestrial environmental changes in NW Europe preceding carbon release at the Paleocene–Eocene transition, Earth Planet. Sc. Lett., 353–354, 108–120, doi:10.1016/j.epsl.2012.08.011, 2012.

Kiehl, J. T. and Shields, C. A.: Sensitivity of the Palaeocene–Eocene Thermal Maximum climate to cloud properties, Philos. T. R. Soc. A, 371, 20130093, doi:10.1098/Rsta.2013.0093, 2013.

Knutti, R. and Sedlacek, J.: Robustness and uncertainties in the new CMIP5 climate model projections, Nature Climate Change, 3, 369–373, doi:10.1038/Nclimate1716, 2013.

Kraus, M. J., McInerney, F. A., Wing, S. L., Secord, R., Baczynski, A. A., and Bloch, J. I.: Paleohydrologic response to continental warming during the Paleocene–Eocene Thermal Maximum, Bighorn Basin, Wyoming, Palaeogeogr. Palaeocl., 370, 196–208, doi:10.1016/j.palaeo.2012.12.008, 2013.

Krishnan, S., Pagani, M., Huber, M., and Sluijs, A.: High latitude hydrological changes during the Eocene Thermal Maximum 2, Earth Planet. Sc. Lett., 404, 167–177, doi:10.1016/j.epsl.2014.07.029, 2014.

CPD
11, 3277–3339, 2015

Kump, L. R. and Pollard, D.: Amplification of Cretaceous warmth by biological cloud feedbacks, Science, 320, 195, doi:10.1126/science.1153883, 2008.

Legates, D. R. and Willmott, C. J.: Mean seasonal and spatial variability in gauge-corrected, global precipitation, Int. J. Climatol., 10, 111–127, doi:10.1002/joc.3370100202, 1990.

Licht, A., van Cappelle, M., Abels, H. A., Ladant, J.-B., Trabucho-Alexandre, J., France-Lanord, C., Donnadieu, Y., Vandenberghe, J., Rigaudier, T., Lecuyer, C., Terry Jr, D., Adriaens, R., Boura, A., Guo, Z., Soe, A. N., Quade, J., Dupont-Nivet, G., Jaeger, J.-J., and Jaeger, J.-J.: Asian monsoons in a late Eocene greenhouse world, Nature, 513, 501–506, doi:10.1038/nature13704, 2014.

Liu, Z., Pagani, M., Zinniker, D., Deconto, R., Huber, M., Brinkhuis, H., Shah, S. R., Leckie, R. M., and Pearson, A.: Global cooling during the eocene-oligocene climate transition, Science, 323, 1187–1190, doi:10.1126/science.1166368, 2009.

Loptson, C. A., Lunt, D. J., and Francis, J. E.: Investigating vegetation–climate feedbacks during the early Eocene, Clim. Past, 10, 419–436, doi:10.5194/cp-10-419-2014, 2014.

Lowenstein, T. K. and Demicco, R. V.: Elevated Eocene atmospheric CO_2 and its subsequent decline, Science, 313, 1928, doi:10.1126/science.1129555, 2006.

Lunt, D. J., Valdes, P. J., Jones, T. D., Ridgwell, A., Haywood, A. M., Schmidt, D. N., Marsh, R., and Maslin, M.: CO_2-driven ocean circulation changes as an amplifier of Paleocene–Eocene Thermal Maximum hydrate destabilization, Geology, 38, 875–878, doi:10.1130/G31184.1, 2010.

Lunt, D. J., Dunkley Jones, T., Heinemann, M., Huber, M., LeGrande, A., Winguth, A., Loptson, C., Marotzke, J., Roberts, C. D., Tindall, J., Valdes, P., and Winguth, C.: A model–data comparison for a multi-model ensemble of early Eocene atmosphere–ocean simulations: EoMIP, Clim. Past, 8, 1717–1736, doi:10.5194/cp-8-1717-2012, 2012.

Markwick, P. J.: Fossil crocodilians as indicators of Late Cretaceous and Cenozoic climates: implications for using palaeontological data in reconstructing palaeoclimate, Palaeogeogr. Palaeocl., 137, 205–271, doi:10.1016/S0031-0182(97)00108-9, 1998.

Mosbrugger, V. and Utescher, T.: The coexistence approach – a method for quantitative reconstructions of Tertiary terrestrial palaeoclimate data using plant fossils, Palaeogeogr. Palaeocl., 134, 61–86, doi:10.1016/S0031-0182(96)00154-X, 1997.

Mosbrugger, V., Utescher, T., and Dilcher, D. L.: Cenozoic continental climatic evolution of Central Europe, P. Natl. Acad. Sci. USA, 102, 14964–14969, doi:10.1073/pnas.0505267102, 2005.

CPD
11, 3277–3339, 2015

Oleson, K. W., Dai, Y., Bonan, G. B., Bosilovich, M., Dickinson, R. E., Dirmeyer, P., Hoffman, F., Houser, P., Levis, S., Niu, G.-Y., Thornton, P., Vertenstein, M., Yang, Z.-L., and Zeng, X. : Technical Description of the Community Land Model (CLM), NCAR Technical Note, NCAR/TN-46, 186, Boulder, CO., doi:10.5065/D6N877R0, 2004.

Pagani, M., Pedentchouk, N., Huber, M., Sluijs, A., Schouten, S., Brinkhuis, H., Sinninghe Damsté, J. S., and Dickens, G. R.: Arctic hydrology during global warming at the Palaeocene/Eocene Thermal Maximum, Nature, 442, 671–675, doi:10.1038/Nature05043, 2006.

Pagani, M., Huber, M., and Sageman, B.: Greenhouse climates, in: Treatise on Geochemistry, 2nd edn., Vol. 6, 281–304, Elsevier Ltd. Amsterdam, doi:10.1016/B978-0-08-095975-7.01314-0, 2013.

Pancost, R. D., Taylor, K. W. R., Inglis, G. N., Kennedy, E. M., Handley, L., Hollis, C. J., Crouch, E. M., Pross, J., Huber, M., Schouten, S., Pearson, P. N., Morgans, H. E. G., and Raine, J. I.: Early Paleogene evolution of terrestrial climate in the SW Pacific, Southern New Zealand, Geochem. Geophy. Geosy., 14, 5413–5429, doi:10.1002/2013gc004935, 2013.

Pearson, P. N., van Dongen, B. E., Nicholas, C. J., Pancost, R. D., Schouten, S., Singano, J. M., and Wade, B. S.: Stable warm tropical climate through the Eocene Epoch, Geology, 35, 211–214, doi:10.1130/G23175A.1, 2007.

Peppe, D. J., Royer, D. L., Cariglino, B., Oliver, S. Y., Newman, S., Leight, E., Enikolopov, G., Fernandez-Burgos, M., Herrera, F., Adams, J.M., Correa, E., Currano, E. D., Erickson, J. M., Hinojosa, L. F., Hoganson, J. W., Iglesias, A., Jaramillo, C. A., Johnson, K. R., Jordan, G. J., Kraft, N. J. B., Lovelock, E. C., Lusk, C. H., Niinemets, Ü., Peñuelas, J., Rapson, G., Wing, S. L., and Wright, I. J.: Sensitivity of leaf size and shape to climate: global patterns and paleoclimatic applications, New Phytol., 190, 724–739, doi:10.1111/j.1469-8137.2010.03615.x, 2011.

Pierrehumbert, R. T.: The hydrologic cycle in deep-time climate problems, Nature, 419, 191–198, 2002.

Poole, I., Cantrill, D., and Utescher, T.: A multi-proxy approach to determine Antarctic terrestrial palaeoclimate during the Late Cretaceous and Early Tertiary, Palaeogeogr. Palaeocl., 222, 95–121, doi:10.1016/j.palaeo.2005.03.011, 2005.

Pross, J., Contreras, L., Bijl, P. K., Greenwood, D. R., Bohaty, S. M., Schouten, S., Bendle, J. A., Rohl, U., Tauxe, L., Raine, J. I., Huck, C. E., van de Flierdt, T., Jamieson, S. S. R., Stickley, C. E., van de Schootbrugge, B., Escutia, C., Brinkhuis, H., and IODP Expedition 318 Scientists:

CPD
11, 3277–3339, 2015

Persistent near-tropical warmth on the Antarctic continent during the early Eocene epoch, Nature, 488, 73–77, doi:10.1038/Nature11300, 2012.
Quan, C., Liu, Y. S. C., and Utescher, T.: Eocene monsoon prevalence over China: a paleobotanical perspective, Palaeogeogr. Palaeocl., 365–366, 302–311, doi:10.1016/j.palaeo.2012.09.035, 2012.
Randall, D. A., Wood, R. A., Bony, S., Colman, R., Fichefet, T., Fyfe, J., Kattsov, V., Pitman, A., Shukla, J., Srinivasan, J., Stouffer, R. J., Sumi, A., and Taylor, K. E. : Climate models and their evaluation, in: Climate Change 2007: the Physical Science Basis. Contribution of Working Group I to the Fourth Assessment Report of the Intergovernmental Panel on Climate Change, Cambridge University Press, NY, 591–662, 2007.
Robert, C. and Kennett, J. P.: Antarctic subtropical humid episode at the Paleocene–Eocene boundary: clay-mineral evidence, Geology, 22, 211–214, doi:10.1130/0091-7613(1994)022<0211:Asheat>2.3.Co;2, 1994.
Roberts, C. D., LeGrande, A. N., and Tripati, A. K.: Climate sensitivity to Arctic seaway restriction during the early Paleogene, Earth Planet. Sc. Lett., 286, 576–585, doi:10.1016/j.epsl.2009.07.026, 2009.
Roeckner, E., Bäuml, G., Bonaventura, L., Brokopf, R., Esch, M., Giorgetta, M., Hagemann, S., Kirchner, I., Kornblueh, L., Rhodin, A., Schlese, U., Schulzweida, U., and Tompkins, A.: The atmospheric general circulation model ECHAM5: Part 1: Model description, Deutsches Klimarechenzentrum, Vol. 349, 1–140, available at: https://www.mpimet.mpg.de/fileadmin/publikationen/Reports/max_scirep_349.pdf (last access: 16 July 2015), 2003.
Royer, D. L., Wing, S. L., Beerling, D. J., Jolley, D. W., Koch, P. L., Hickey, L. J., and Berner, R. A.: Paleobotanical evidence for near present-day levels of atmospheric CO_2 during part of the tertiary, Science, 292, 2310–2313, doi:10.1126/science.292.5525.2310, 2001.
Royer, D. L., Wilf, P., Janesko, D. A., Kowalski, E. A., and Dilcher, D. L.: Correlations of climate and plant ecology to leaf size and shape: potential proxies for the fossil record, Am. J. Bot., 92, 1141–1151, doi:10.3732/ajb.92.7.1141, 2005.
Royer, D. L., Sack, L., Wilf, P., Lusk, C. H., Jordan, G. J., Niinemets, Ü., Wright, I. J., Westoby, M., Cariglino, B., Coley, P. D., Cutter, A. D., Johnson, K. R., Labandeira, C. C., Moles, A. T., Palmer, M. B., and Valladares, F.: Fossil leaf economics quantified: calibration, Eocene case study, and implications, Paleobiology, 33, 574–589, doi:10.1666/07001.1, 2007.

CPD
11, 3277–3339, 2015

Sagoo, N., Valdes, P., Flecker, R., and Gregoire, L. J.: The Early Eocene equable climate problem: can perturbations of climate model parameters identify possible solutions?, Philos. T. R. Soc. A, 371, 20130123, doi:10.1098/Rsta.2013.0123, 2013.

Schmidt, G. A., Ruedy, R., Hansen, J. E., Aleinov, I., Bell, N., Bauer, M., Bauer, S., Cairns, B., Canuto, V., Cheng, Y., Del Genio, A., Faluvegi, G., Friend, A. D., Hall, T. M., Hu, Y., Kelley, M., Kiang, N. Y., Koch, D., Lacis, A. A., Lerner, J., Lo, K. K., Miller, R. L., Nazarenko, L., Oinas, V., Perlwitz, J., Perlwitz, J., Rind, D., Romanou, A., Russell, G. L., Sato, M., Shindell, D. T., Stone, P. H., Sun, S., Tausnev, N., Thresher, D., and Yao, M. S.: Present-day atmospheric simulations using GISS ModelE: comparison to in situ, satellite, and reanalysis data, J. Climate, 19, 153–192, doi:10.1175/JCLI3612.1, 2006.

Schmitz, B. and Pujalte, V.: Abrupt increase in seasonal extreme precipitation at the Paleocene–Eocene boundary, Geology, 35, 215–218, doi:10.1130/G23261a.1, 2007.

Schubert, B. A., Jahren, A. H., Eberle, J. J., Sternberg, L. S. L., and Eberth, D. A.: A summertime rainy season in the Arctic forests of the Eocene, Geology, 40, 523–526, doi:10.1130/G32856.1, 2012.

Sewall, J. O., Sloan, L. C., Huber, M., and Wing, S.: Climate sensitivity to changes in land surface characteristics, Global Planet. Change, 26, 445–465, doi:10.1016/S0921-8181(00)00056-4, 2000.

Shellito, C. J. and Sloan, L. C.: Reconstructing a lost Eocene Paradise, Part II: On the utility of dynamic global vegetation models in pre-Quaternary climate studies, Global Planet. Change, 50, 18–32, doi:10.1016/j.gloplacha.2005.08.002, 2006.

Shellito, C. J., Lamarque, J. F., and Sloan, L. C.: Early Eocene Arctic climate sensitivity to pCO_2 and basin geography, Geophys. Res. Lett., 36, L09707, doi:10.1029/2009gl037248, 2009.

Sloan, L. C., Walker, J. C., Moore, T. C., Rea, D. K., and Zachos, J. C.: Possible methane-induced polar warming in the early Eocene, Nature, 357, 320–322, doi:10.1038/357320a0, 1992.

Sluijs, A., Schouten, S., Pagani, M., Woltering, M., Brinkhuis, H., Damste, J. S. S., Dickens, G. R., Huber, M., Reichart, G. J., Stein, R., Matthiessen, J., Lourens, L. J., Pedentchouk, N., Backman, J., Moran, K., and Expedition 302 Scientists: Subtropical arctic ocean temperatures during the Palaeocene/Eocene thermal maximum, Nature, 441, 610–613, doi:10.1038/Nature04668, 2006.

Sluijs, A., Bowen, G. J., Brinkhuis, H., Lourens, L. J., and Thomas, E.: The Palaeocene-Eocene Thermal Maximum super greenhouse: biotic and geochemical signatures, age models and

CPD
11, 3277–3339, 2015

mechanisms of global change, in: Deep-Time Perspectives on Climate Change: Marrying the Signal from Computer Models and Biological Proxies, edited by: Williams, M., Haywood, A. M., Gregory, F. J., and Schmidt, D. N., The Geological Society, Bath, 323–350, 2007.
Smith, F., Wing, S., and Freeman, K.: Magnitude of the carbon isotope excursion at the Paleocene–Eocene thermal maximum: the role of plant community change, Earth Planet. Sc. Lett., 262, 50–65, doi:10.1016/j.epsl.2007.07.021, 2007.
Smith, R. S. and Gregory, J.: The last glacial cycle: transient simulations with an AOGCM, Clim. Dynam., 38, 1545–1559, doi:10.1007/s00382-011-1283-y, 2012.
Smith, R. S., Gregory, J. M., and Osprey, A.: A description of the FAMOUS (version XDBUA) climate model and control run, Geosci. Model Dev., 1, 53–68, doi:10.5194/gmd-1-53-2008, 2008.
Smith, R. Y., Greenwood, D. R., and Basinger, J. F.: Estimating paleoatmospheric pCO_2 during the Early Eocene Climatic Optimum from stomatal frequency of Ginkgo, Okanagan Highlands, British Columbia, Canada, Palaeogeogr. Palaeocl., 293, 120–131, doi:10.1016/j.palaeo.2010.05.006, 2010.
Smith, R. Y., Basinger, J. F., and Greenwood, D. R.: Early Eocene plant diversity and dynamics in the Falkland flora, Okanagan Highlands, British Columbia, Canada, Palaeobiodiversity and Palaeoenvironments, 92, 309–328, doi:10.1007/s12549-011-0061-5, 2012.
Speelman, E. N., Sewall, J. O., Noone, D., Huber, M., von der Heydt, A., Damste, J. S., and Reichart, G. J.: Modeling the influence of a reduced equator-to-pole sea surface temperature gradient on the distribution of water isotopes in the Early/Middle Eocene, Earth Planet. Sc. Lett., 298, 57–65, doi:10.1016/j.epsl.2010.07.026, 2010.
Storey, M., Duncan, R. A., and Swisher, C. C.: Paleocene–Eocene Thermal Maximum and the opening of the Northeast Atlantic, Science, 316, 587–589, doi:10.1126/science.1135274, 2007.
Sturm, C., Zhang, Q., and Noone, D.: An introduction to stable water isotopes in climate models: benefits of forward proxy modelling for paleoclimatology, Clim. Past, 6, 115–129, doi:10.5194/cp-6-115-2010, 2010.
Suarez, M. B., Gonzalez, L. A., Ludvigson, G. A., Vega, F. J., and Alvarado-Ortega, J.: Isotopic composition of low-latitude paleoprecipitation during the Early Cretaceous, Geol. Soc. Am. Bull., 121, 1584–1595, doi:10.1130/B26453.1, 2009.
Sun, X. and Wang, P.: How old is the Asian monsoon system? – Palaeobotanical records from China, Palaeogeogr. Palaeocl., 222, 181–222, doi:10.1016/j.palaeo.2005.03.005, 2005.

CPD
11, 3277–3339, 2015

Sunderlin, D., Loope, G., Parker, N. E., and Williams, C. J.: Paleoclimatic and paleoecological implications of a Paleocene–Eocene fossil leaf assemblage, Chickaloon Formation, Alaska, Palaios, 26, 335–345, doi:10.2110/palo.2010.p10-077r, 2011.

Sunderlin, D., Trop, J. M., Idleman, B. D., Brannick, A., White, J. G., and Grande, L.: Paleoenvironment and paleoecology of a Late Paleocene high-latitude terrestrial succession, Arkose Ridge Formation at Box Canyon, southern Talkeetna Mountains, Alaska, Palaeogeogr. Palaeocl., 401, 57–80, doi:10.1016/j.palaeo.2014.02.012, 2014.

Svensen, H., Planke, S., Malthe-Sørenssen, A., Jamtveit, B., Myklebust, R., Rasmussen Eidem, T., and Rey, S. S.: Release of methane from a volcanic basin as a mechanism for initial Eocene global warming, Nature, 429, 542–545, doi:10.1038/nature02566, 2004.

Taylor, K. E., Stouffer, R. J., and Meehl, G. A.: An overview of CMIP5 and the experiment design, B. Am. Meteorol. Soc., 93, 485–498, doi:10.1175/BAMS-D-11-00094.1, 2012.

Taylor, K. W. R., Huber, M., Hollis, C. J., Hernandez-Sanchez, M. T., and Pancost, R. D.: Re-evaluating modern and Palaeogene GDGT distributions: implications for SST reconstructions, Global Planet. Change, 108, 158–174, doi:10.1016/j.gloplacha.2013.06.011, 2013.

Tindall, J., Flecker, R., Valdes, P., Schmidt, D. N., Markwick, P., and Harris, J.: Modelling the oxygen isotope distribution of ancient seawater using a coupled ocean–atmosphere GCM: implications for reconstructing early Eocene climate, Earth Planet. Sc. Lett., 292, 265–273, doi:10.1016/j.epsl.2009.12.049, 2010.

Tipple, B. J., Berke, M. A., Doman, C. E., Khachaturyan, S., and Ehleringer, J. R.: Leaf-wax n-alkanes record the plant–water environment at leaf flush, P. Natl. Acad. Sci. USA, 110, 2659–2664, doi:10.1073/pnas.1213875110, 2013.

Trenberth, K. E.: Changes in precipitation with climate change, Clim. Res., 47, 123–138, doi:10.3354/cr00953, 2011.

Turner, A. G. and Slingo, J. M.: Uncertainties in future projections of extreme precipitation in the Indian monsoon region, Atmos. Sci. Lett., 10, 152–158, doi:10.1002/asl.223, 2009.

Uhl, D., Traiser, C., Griesser, U., and Denk, T.: Fossil leaves as palaeoclimate proxies in the Palaeogene of Spitsbergen (Svalbard), Acta Palaeobotanica, 47, 89–107, 2007.

Valdes, P.: Built for stability, Nat. Geosci., 4, 414–416, doi:10.1038/ngeo1200, 2011.

Waddell, L. M. and Moore, T. C.: Salinity of the Eocene Arctic Ocean from oxygen isotope analysis of fish bone carbonate, Paleoceanography, 23, PA1S12, doi:10.1029/2007PA001451, 2008.

CPD
11, 3277–3339, 2015

Wang, D., Lu, S., Han, S., Sun, X., and Quan, C.: Eocene prevalence of monsoon-like climate over eastern China reflected by hydrological dynamics, J. Asian Earth Sci., 62, 776–787, doi:10.1016/j.jseaes.2012.11.032, 2013.

White, T., Gonzalez, L., Ludvigson, G., and Poulsen, C.: Middle Cretaceous greenhouse hydrologic cycle of North America, Geology, 29, 363–366, doi:10.1130/0091-7613(2001)029<0363:Mcghco>2.0.Co;2, 2001.

Wilf, P.: Late Paleocene–Early Eocene climate changes in southwestern Wyoming: paleobotanical analysis, Geol. Soc. Am. Bull., 112, 292–307, doi:10.1130/0016-7606(2000)112<0292:Lpeecc>2.3.Co;2, 2000.

Wilf, P., Wing, S. L., Greenwood, D. R., and Greenwood, C. L.: Using fossil leaves as paleoprecipitation indicators: an Eocene example, Geology, 26, 203–206, doi:10.1130/0091-7613(1998)026<0203:UFLAPI>2.3.Co;2, 1998.

Wilf, P., Johnson, K. R., Cuneo, N. R., Smith, M. E., Singer, B. S., and Gandolfo, M. A.: Eocene plant diversity at Laguna del Hunco and Rio Pichileufu, Patagonia, Argentina, Am. Nat., 165, 634–650, doi:10.1086/430055, 2005.

Williams, J. H. T., Smith, R. S., Valdes, P. J., Booth, B. B. B., and Osprey, A.: Optimising the FAMOUS climate model: inclusion of global carbon cycling, Geosci. Model Dev., 6, 141–160, doi:10.5194/gmd-6-141-2013, 2013.

Wing, S. L. and Greenwood, D. R.: Fossils and fossil climate – the case for equable continental interiors in the Eocene, Philos. T. Roy. Soc. B, 341, 243–252, doi:10.1098/rstb.1993.0109, 1993.

Wing, S. L., Harrington, G. J., Smith, F. A., Bloch, J. I., Boyer, D. M., and Freeman, K. H.: Transient floral change and rapid global warming at the Paleocene–Eocene boundary, Science, 310, 993–996, doi:10.1126/science.1116913, 2005.

Wing, S. L., Herrera, F., Jaramillo, C. A., Gómez-Navarro, C., Wilf, P., and Labandeira, C. C.: Late Paleocene fossils from the Cerrejon Formation, Colombia, are the earliest record of Neotropical rainforest, P. Natl. Acad. Sci. USA, 106, 18627–18632, doi:10.1073/pnas.0905130106, 2009.

Winguth, A., Shellito, C., Shields, C., and Winguth, C.: Climate response at the Paleocene–Eocene Thermal Maximum to greenhouse gas forcing – a model study with CCSM3, J. Climate, 23, 2562–2584, doi:10.1175/2009jcli3113.1, 2010.

CPD
11, 3277–3339, 2015

Winguth, A. M. E., Thomas, E., and Winguth, C.: Global decline in ocean ventilation, oxygenation, and productivity during the Paleocene–Eocene Thermal Maximum: implications for the benthic extinction, Geology, 40, 263–266, doi:10.1130/G32529.1, 2012.

Wolfe, J. A.: A method of obtaining climatic parameters from leaf assemblages, US Geological Survey Bulletin, United States Government Printing Office, Washington, 2040, 1–71, 1993.

Yapp, C. J.: Fe(CO_3)OH in goethite from a mid-latitude North American Oxisol: estimate of atmospheric CO_2 concentration in the Early Eocene "climatic optimum", Geochim. Cosmochim. Ac., 68, 935–947, doi:10.1016/j.gca.2003.09.002, 2004.

Yin, X., Gruber, A., and Arkin, P.: Comparison of the GPCP and CMAP merged gauge–satellite monthly precipitation products for the period 1979–2001, J. Hydrometeorol., doi:10.1175/JHM-392.1, 2004.

Zachos, J. C., Schouten, S., Bohaty, S., Quattlebaum, T., Sluijs, A., Brinkhuis, H., Gibbs, S. J., and Bralower, T. J.: Extreme warming of mid-latitude coastal ocean during the Paleocene–Eocene Thermal Maximum: inferences from TEX86 and isotope data, Geology, 34, 737–740, doi:10.1130/G22522.1, 2006.

Zachos, J. C., Dickens, G. R., and Zeebe, R. E.: An early Cenozoic perspective on greenhouse warming and carbon-cycle dynamics, Nature, 451, 279–283, 2008.

Zacke, A., Voigt, S., Joachimski, M. M., Gale, A. S., Ward, D. J., and Tutken, T.: Surface-water freshening and high-latitude river discharge in the Eocene North Sea. J. Geol. Soc. London, 166, 969–980, doi:10.1144/0016-76492008-068, 2009.

Zhang, S. and Wang, B.: Global summer monsoon rainy seasons, Int. J. Climatol., 28, 1563–1578, doi:10.1002/joc.1659, 2008.

CPD
11, 3277–3339, 2015

Table 1. Summary of model simulations in the ensemble adapted from Table 1 of Lunt et al. (2012). Additions detailing precipitation schemes are from Table 2 of Dai (2006). Some models have irregular grids in the atmosphere and/or ocean, or have spectral atmospheres. The atmospheric and ocean resolution are given in number of gridboxes, $X \times Y \times Z$ where X is the effective number of gridboxes in the zonal, Y in the meridional, and Z in the vertical.

Model	Eocene simulation reference	Model reference	Atmosphere resolution	Ocean resolution	Paleogeography	Sim. length (years)	CO_2 levels
HadCM3L HadCM3L (T)	Lunt et al. (2010) Loptson et al. (2014)	Cox et al. (2001)	96 × 73 × 19	96 × 73 × 20	Proprietary	> 3400	×1,2,4,6 ×2,4
ECHAM5	Heinemann et al. (2009)	Roeckner et al. (2003)	96 × 48 × 19	142 × 82 × 40	Bice and Marotzke (2001)	2500	×2
CCSM3 (W)	Winguth et al. (2010, 2012)	Collins et al. (2006); Yeager et al. (2006)	96 × 48 × 26	100 × 116 × 25	Sewall et al. (2000) with marginal sea parameterisation	1500	×4,8,16
CCSM3 (H)	Liu et al. (2009); Huber and Caballero (2011)	Collins et al. (2006); Yeager et al. (2006)	96 × 48 × 26	100 × 122 × 25	Sewall et al. (2000)	1500	×2,4,8,16
CCSM3 (K)	Kiehl and Shields (2013)	Collins et al. (2006); Yeager et al. (2006)	96 × 48 × 26	100 × 116 × 25	As CCSM W	> 2000 > 3600+	× ~ 5 × ~ 9
GISS E-R	Roberts et al. (2009)	Schmidt et al. (2006)	72 × 45 × 20	72 × 45 × 13	Bice and Marotzke (2001)	2000	× ~ 4
FAMOUS	Sagoo et al. (2013)	Jones et al. (2005), Smith et al. (2008)	48 × 37 × 11	96 × 73 × 20	Proprietary	> 1500	×2

Model	Stratiform precipitation	Convective precipitation	Vegetation	Aerosols
HadCM3	Large-scale precipitation is calculated based on cloud water and ice contents (similar to Smith, 1990)	Bulk mass flux scheme (Gregory and Rowntree, 1990), with improvement by Gregory et al. (1997)	Homogenous shrubland (Lunt) Dynamically evolving vegetation TRIFFID (Loptson)	As control
ECHAM5	Prognostic equations for the water phases, bulk cloud microphysics (Lohmann and Roeckner, 1996)	Bulk mass flux scheme (Tiedtke, 1989) with modifications for deep convection according to Nordeng (1994)	Homogenous woody savannah	As control
CCSM_W	Prognostic condensate and precipitation parameterisation (Zhang et al., 2003)	Simplified Arakawa and Schubert (1974) (cumulus ensemble) scheme developed by Zhang and McFarlane (1995)	Shellito and Sloan (2006)	As control
CCSM_H			Sewall et al. (2000)	Reduced aerosol loading.
CCSM_K			Sewall et al. (2000)	Cloud microphysical parameters altered
GISS E-R	Prognostic stratiform cloud based on moisture convergence (Del Genio et al., 1996)	Bulk mass flux scheme by Del Genio and Yao (1993)	Sewall et al. (2000)	As control
FAMOUS	Precipitation parameterisation schemes are based on those of HadCM3		Homogenous shrubland	Uncertain perturbed parameters include those relating to cloud microphysical properties

CPD
11, 3277–3339, 2015

Table 2. Summary of relationships between global Surface Air Temperature and precipitation rate.

Model simulations	*P*-*T* regression[a]	% increase *P* per ˚C warming over range[b]
HadCM3L	$P = 0.0542T + 2.1747$	1.81
HadCM3L(T)	$P = 0.0398T + 2.4278$	1.32
CCSM3_H	$P = 0.0594T + 2.0506$	2.02
CCSM3_K	$P = 0.0628T + 1.9739$	2.15
CCSM3_W	$P = 0.0596T + 1.9341$	2.11
FAMOUS	$P = 0.0774T + 1.6006$	2.80

[a] T = SAT˚C, P = global precipitation mm day^{-1}.
[b] Precipitation sensitivity is calculated over the range of 15–30˚C.

CPD
11, 3277–3339, 2015

Table 3. % land surface characterised by extended summer precipitation > 55 % MA.

Model	PI	×1 CO_2	×2 CO_2	×4/5 CO_2	×6/8/9 CO_2	×16 CO_2
HadCM3L	60.1	66.3	62.6	57.7	52.3	
HadCM3L(T)			62.0	51.6		
ECHAM5	50.1		41.6			
GISS E-R	47.7			37.6		
CCSM(H)	50.1		47.3	44.2	42.4	35.1
CCSM(K)				47.5	34.12	
FAMOUS	48.9		28.1 E16 23.6 E17			

CPD
11, 3277–3339, 2015

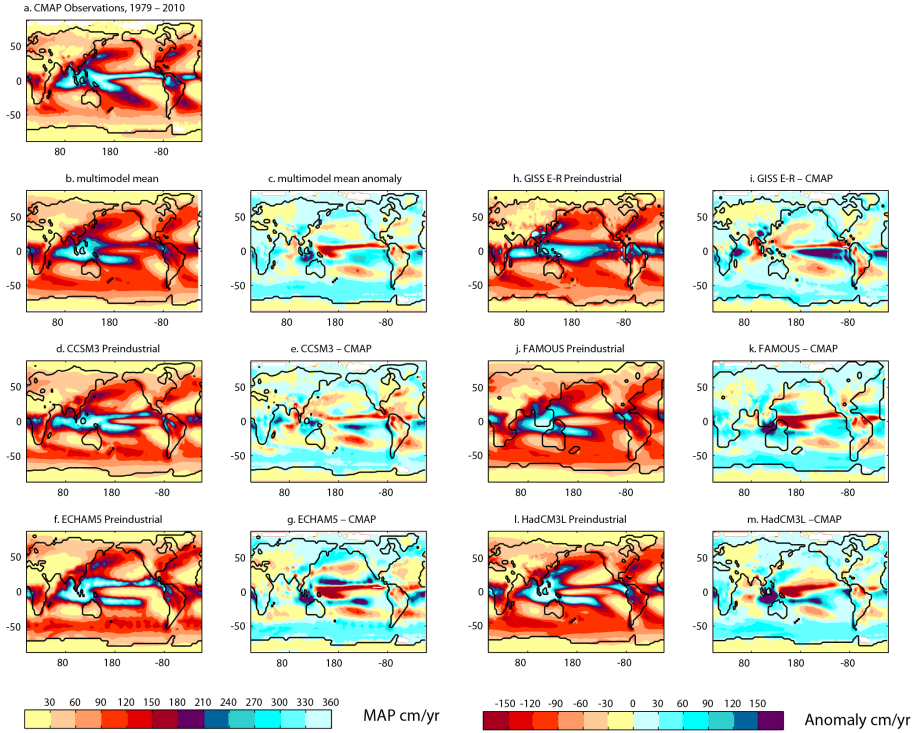

Figure 1. Preindustrial precipitation distributions as simulated in the EoMIP models. (**a**, **b**, **d**, **f**, **h**, **j** and **l**) show Mean Annual Precipitation (MAP; left colour bar) and (**c**, **e**, **g**, **i**, **k**, and **m**) show anomalies relative to CMAP observations, 1979–2010, GCM output – observations (right colour bar).

CPD
11, 3277–3339, 2015

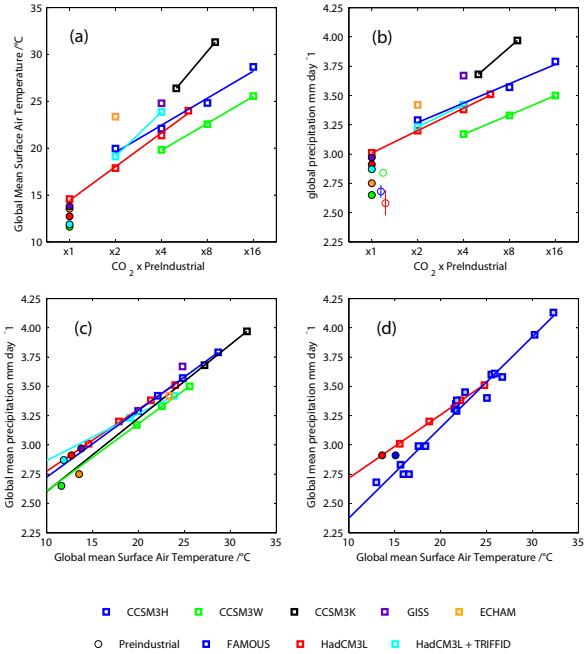

Figure 2. Global sensitivity of the Eocene hydrological cycle in the EoMIP simulations. Global mean surface air temperature relative to model CO_2 **(a)**, global mean precipitation rate relative to model CO_2 **(b)** and global mean surface air temperature **(c)**; note the logarithmic scale on the horizontal axis in (**a** and **b**). Preindustrial simulations and Eocene simulations are shown as circles and squares respectively. The CCSM3 simulations share a preindustrial simulation, shown in green. Open circle symbols in **(b)** show modern day estimates of global precipitation rate calculated based on CMAP data (red), GPCP data (blue) and Legates and Willmott (1990) climatology (green). Also shown is the sensitivity of the hydrological cycle to global mean Surface Air Temperature in the 17 successful simulations of Sagoo et al. (2013) using FAMOUS (**d**; blue squares), with HadCM3L simulations (red; Lunt et al., 2010) shown for comparison. All best fit lines are based on Eocene simulations only.

CPD
11, 3277–3339, 2015

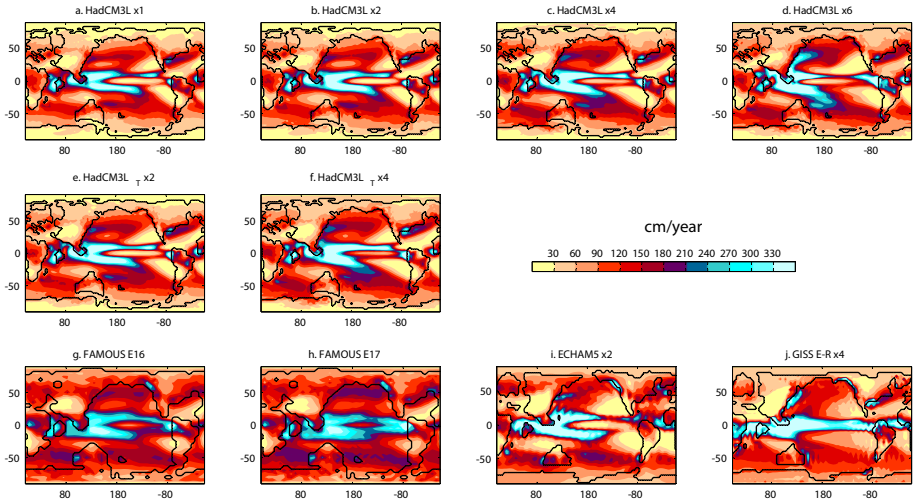

Figure 3.

CPD
11, 3277–3339, 2015

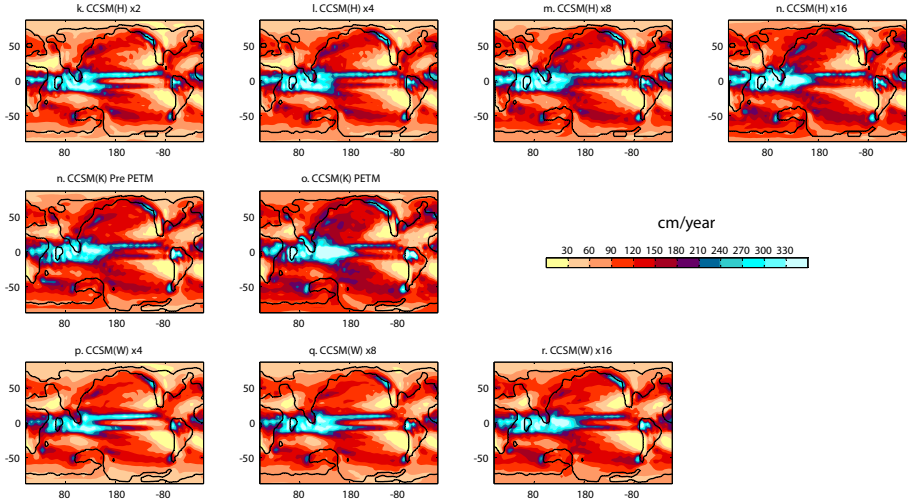

Figure 3. Mean annual precipitation distributions for each member of the EoMIP ensemble in cm year^{-1}. CO_2 for each model simulation is shown above each plot. The FAMOUS simulations are both at $2 \times CO_2$.

CPD
11, 3277–3339, 2015

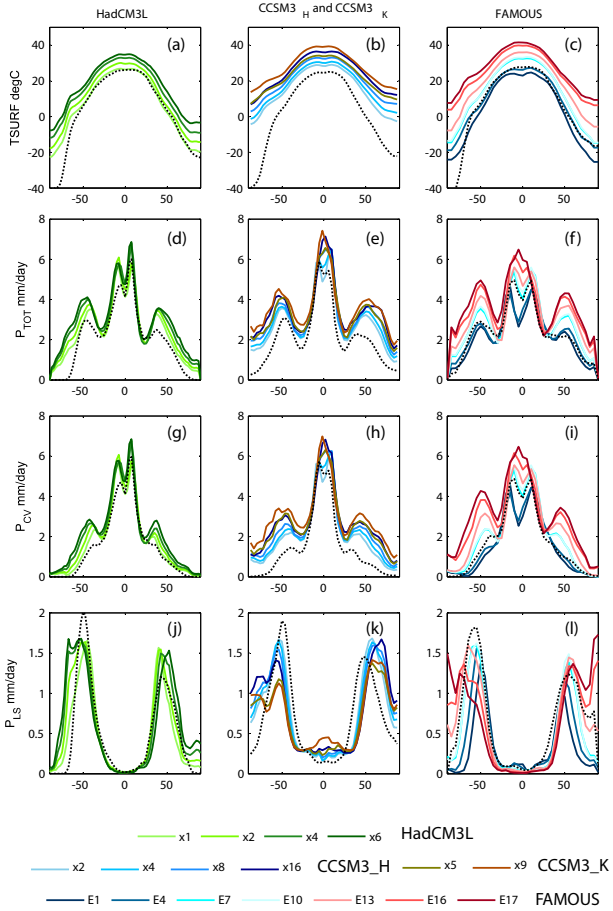

CPD
11, 3277–3339, 2015

Insights into the early Eocene hydrological cycle

M. J. Carmichael et al.

Figure 4. Latitudinal temperature and precipitation distributions in the HadCM3L (left), CCSM3_H and CCSM3_K (centre) and FAMOUS (right) members of the EoMIP ensemble. **(a–c)** show mean surface air temperature, **(d–f)** total precipitation rate, **(g–i)** convective precipitation and **(j–l)** large-scale precipitation. The HadCM3L and CCSM3 atmospheric CO_2 levels are shown in the key. All FAMOUS simulations are at $2 \times$ PI CO_2, but differ in value for 10 uncertain parameters (Sect. 2). Simulation names E1–E17 shown in the legend correspond to those given by Sagoo et al. (2013). Black dotted lines show output from preindustrial simulations.

CPD
11, 3277–3339, 2015

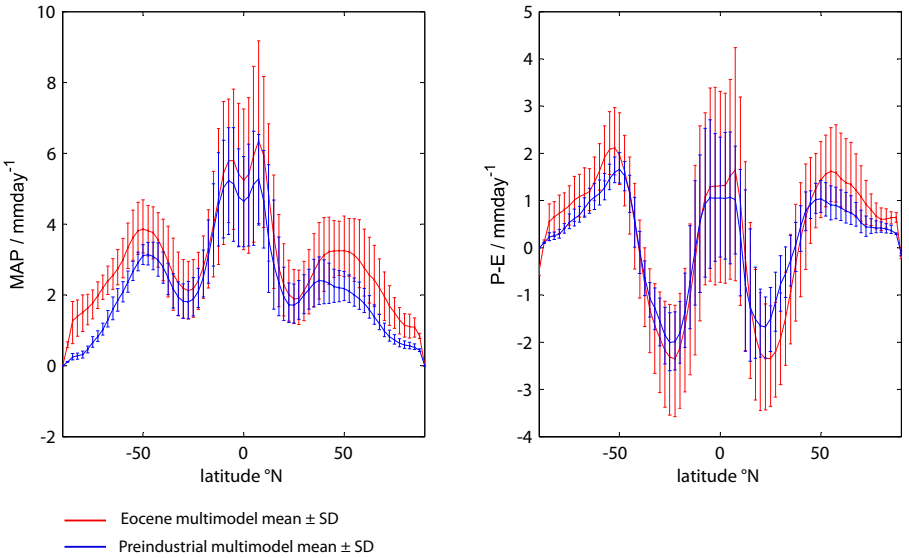

Figure 5. Multimodel Mean Annual Precipitation **(a)** and Mean Annual Precipitation – Evaporation rate **(b)** for Eocene (red) and preindustrial (blue) boundary conditions. For the Eocene multimodel mean, simulations have a global mean precipitation rate of $3.40 \pm 0.02\,\mathrm{mm\,day^{-1}}$ which are: HadCM3L (×4), HadCM3L_T (×4), ECHAM (×2), CCSM3_H (×4) and a linearly interpolated distribution between the ×4 and ×8 CO_2 CCSM3_W simulations. Error bars represent the range in values across simulations.

CPD
11, 3277–3339, 2015

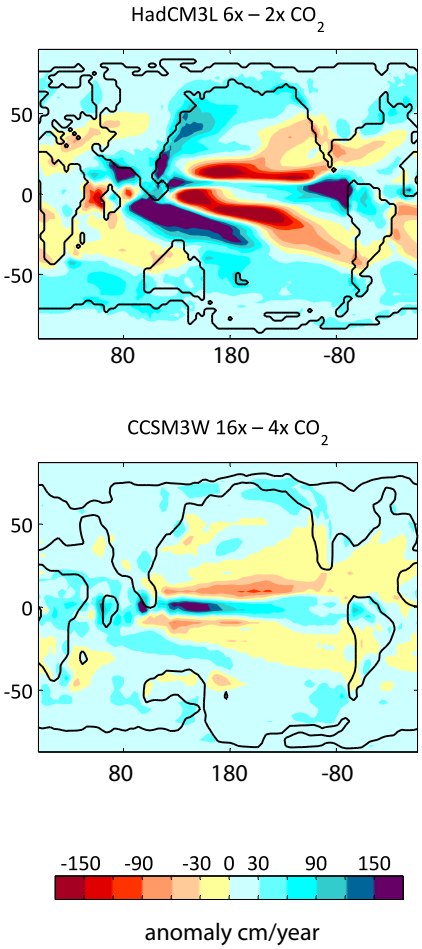

Figure 6. Anomaly plots for Mean Annual Precipitation cm year^{-1} between high and low CO_2 model simulations for **(a)** HadCM3L ×6 CO_2 – ×2 CO_2 and **(b)** CCSM3_W ×16 CO_2 – ×4 CO_2.

CPD
11, 3277–3339, 2015

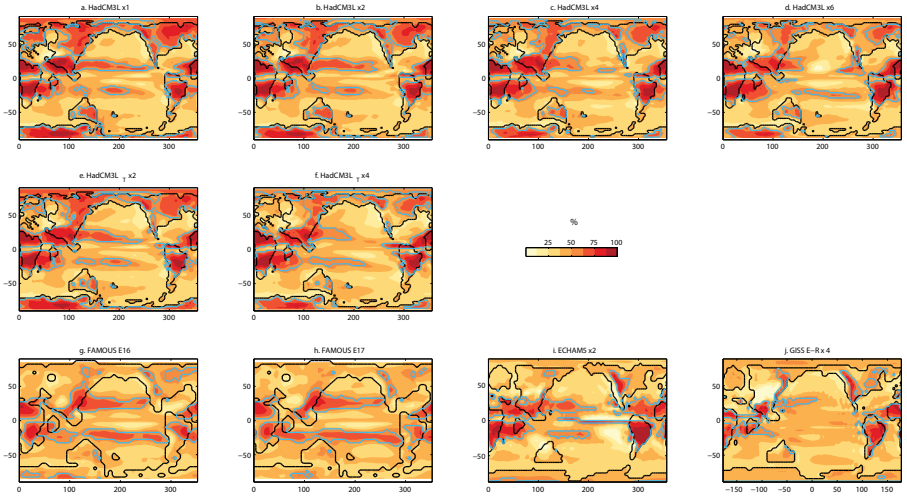

Figure 7.

CPD
11, 3277–3339, 2015

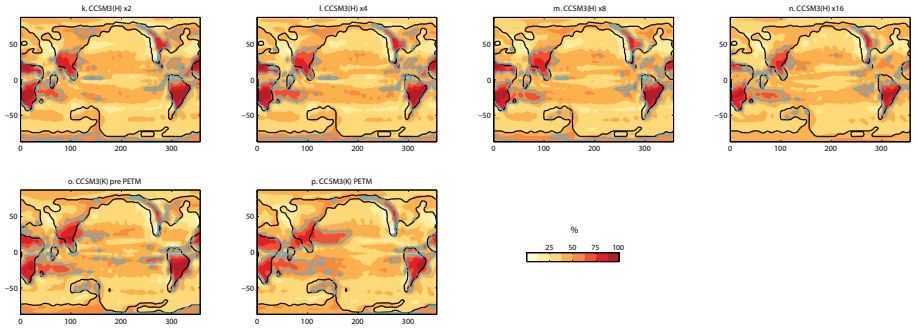

Figure 7. Percentage of mean annual precipitation falling in the extended summer season (MJ-JAS for Northern Hemisphere, NDJFM for Southern Hemisphere); regions with > 55 % summer precipitation are outlined in blue. Results from preindustrial simulations are shown in the Supplement. CO_2 for each model simulation is shown above each plot. The FAMOUS simulations are both at $2 \times CO_2$.

CPD
11, 3277–3339, 2015

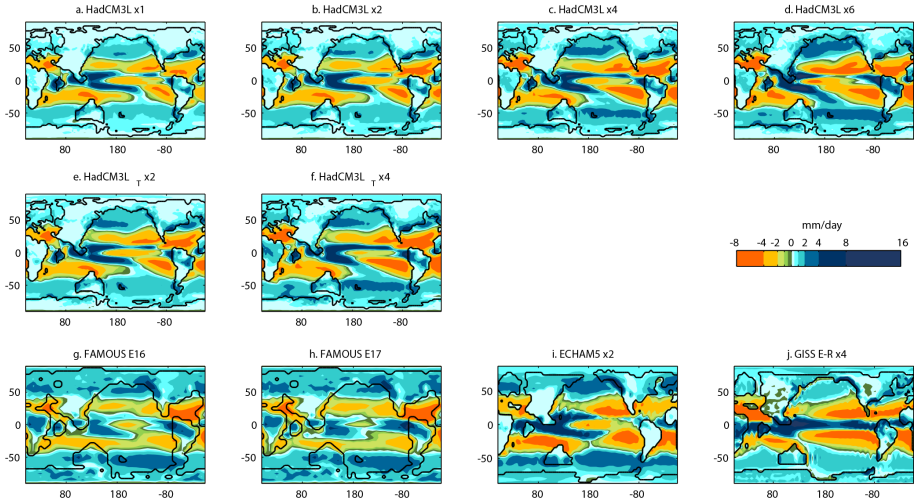

Figure 8.

CPD
11, 3277–3339, 2015

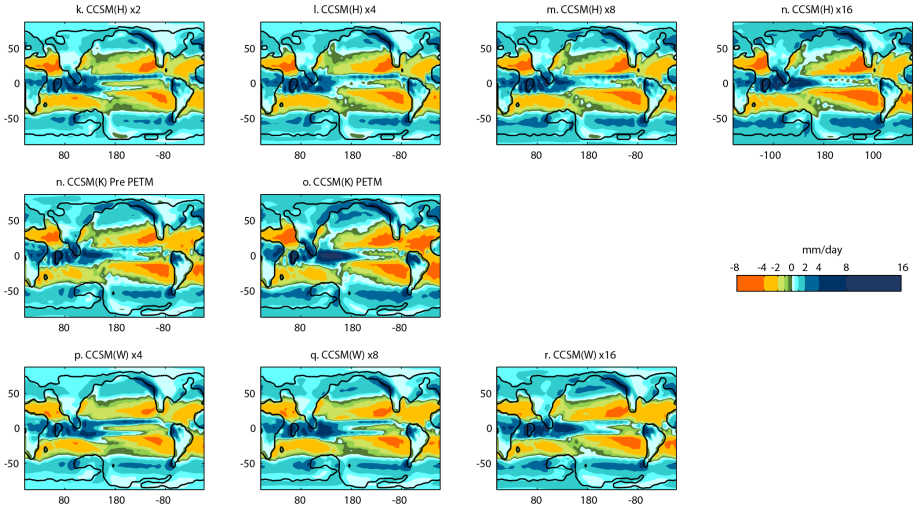

Figure 8. Mean annual $P - E$ distributions for each member of the EoMIP ensemble in mm day^{-1}. CO_2 for each model simulation is shown above each plot. The FAMOUS simulations are both at $2 \times CO_2$.

CPD
11, 3277–3339, 2015

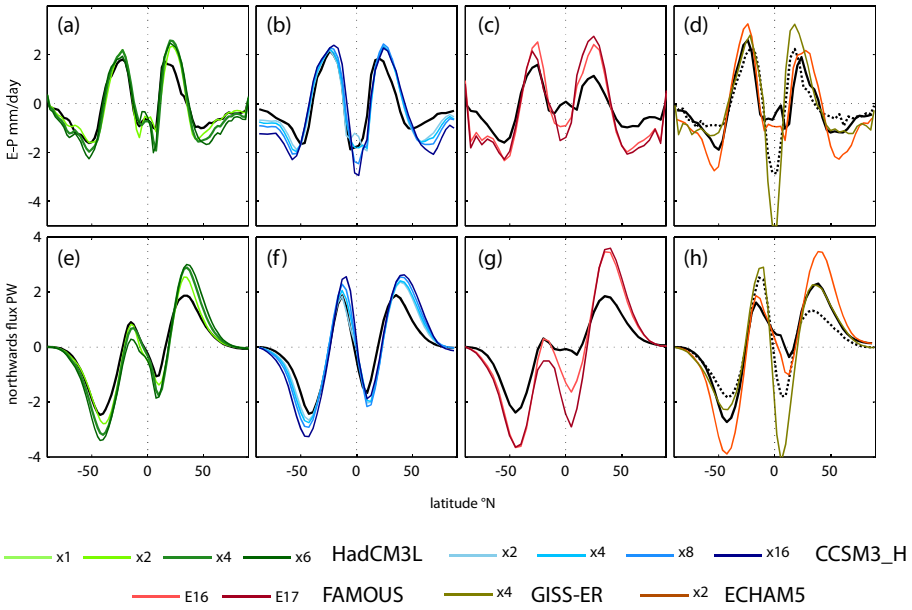

Figure 9. Latitudinal $P - E$ distributions (top) and implied northwards latent heat flux (bottom) in the EoMIP simulations. The black lines indicate preindustrial simulations with dotted and unbroken lines in (**d** and **h**) corresponding to the GISS-ER and ECHAM5 simulations respectively. Heat flux expressed in petawatts (1 PW = 10^{15} W).

CPD
11, 3277–3339, 2015

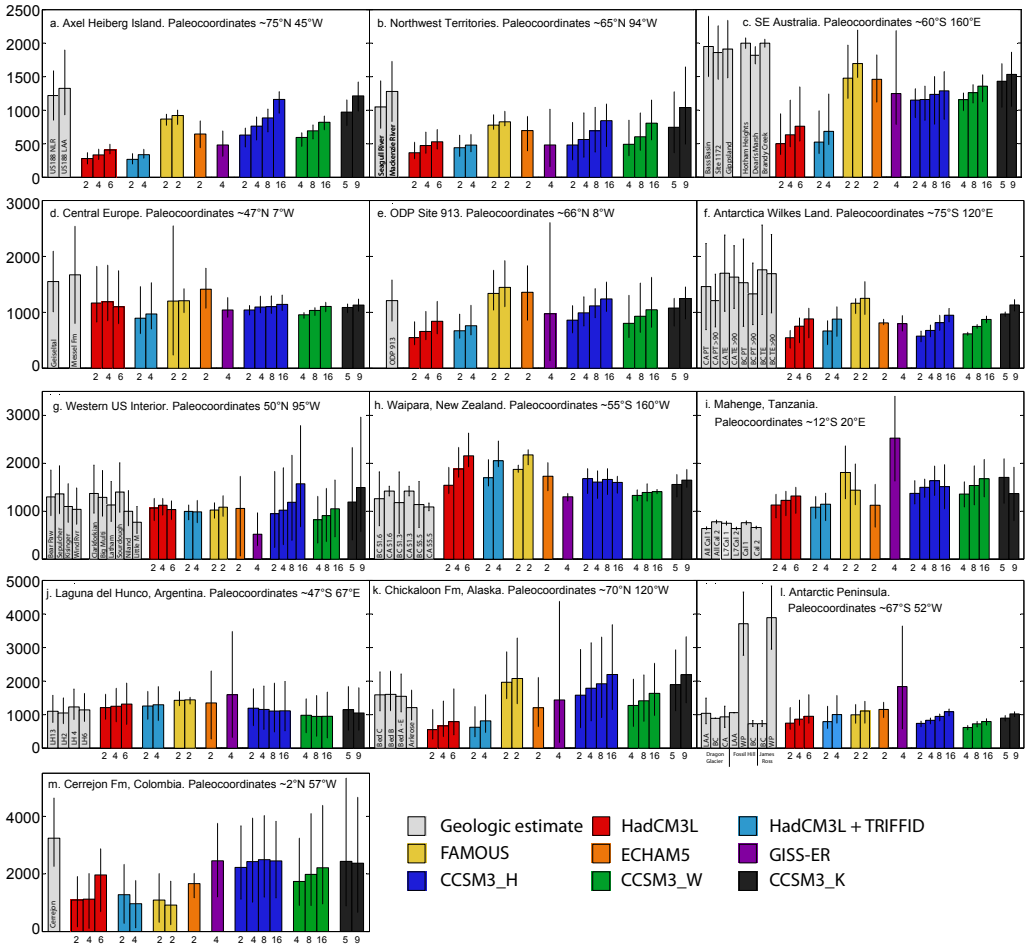

CPD
11, 3277–3339, 2015

Insights into the early Eocene hydrological cycle

M. J. Carmichael et al.

Figure 10. Proxy-model comparisons for Mean Annual Precipitation (MAP) for the EoMIP ensemble **(a)** Axel Heiberg island, data from Greenwood et al. (2010); **(b)** North West Territories, data from Greenwood et al. (2010); **(c)** South East Australia and Tasmania, data from Greenwood et al. (2005) and Contreras et al. 2014); **(d)** central Europe, data from Mosbrugger et al. (2005) and Grein et al. (2011); **(e)** ODP Site 913, data from Eldrett et al. (2009); **(f)** Wilkes Land, data from Pross et al. (2012); **(g)** Western US interior, data from Wilf et al. (1998) and Wilf (2000); **(h)** Waipara, New Zealand, data from Pancost et al. (2013); **(i)** Mahenge, Tanzania, data from Jacobs and Herendeen (2004) and Kaiser et al. (2006); **(j)** Argentina, data from Wilf et al. (2005) **(k)** Chickaloon Fm, Alaska, data from Sunderlin et al. (2011, 2014); **(l)** Antarctic Peninsula, data from Hunt and Poole (2003) and Poole et al. (2005); **(m)** Cerrejon Formation, data from Wing et al. (2009). Error bars show the mean with range based on nine model grid cells closest to given paleocoordinates. Full details are given in the Supplement, Table S3.

CPD
11, 3277–3339, 2015

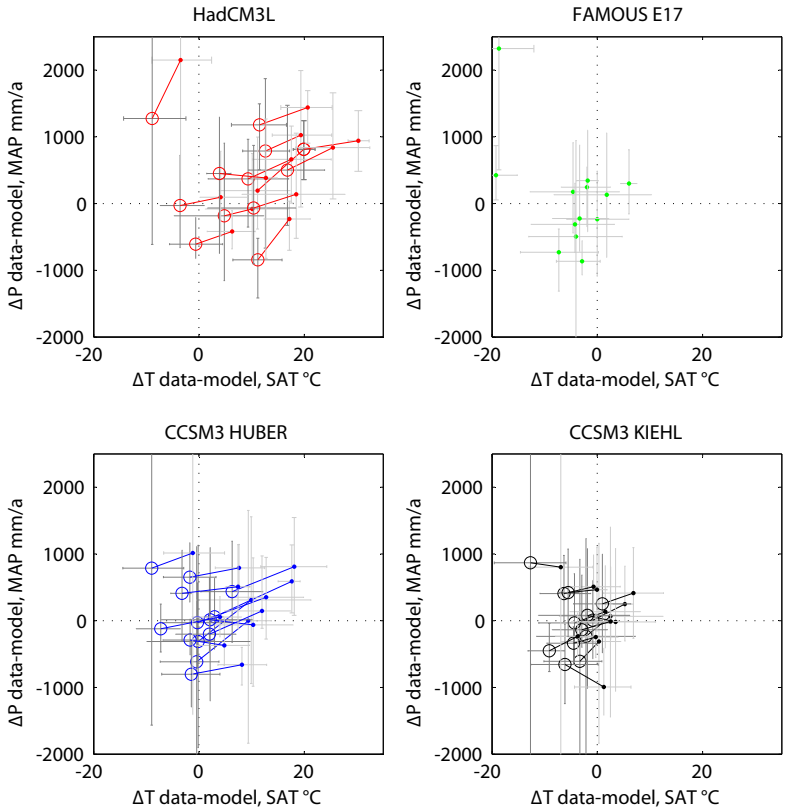

Figure 11. Surface air temperature and mean annual precipitation proxy-model anomalies for low and high CO_2 climates shown by closed and open circles respectively. Simulations are at ×2 and ×6 CO_2 for HadCM3L **(a)**, E17 for FAMOUS **(b)**, ×2 and ×16 CO_2 for CCSM3_H **(c)**, and ×5 and ×9 CO_2 for CCSM3_K **(d)**. The data points represent averaged signals for the sites shown in Fig. 8. Estimates of maximum (minimum) error are calculated as anomalies between the highest (lowest) data estimate and the lowest (highest) value within the local model grid.

CPD
11, 3277–3339, 2015